PCCP
INVITED ARTICLE

Unravelling aspects of the gas phase chemistry involved in diamond chemical vapour deposition

Michael N. R. Ashfold,*[a] Paul W. May,[a] James R. Petherbridge,[a] Keith N. Rosser,[a] James A. Smith,[a] Yuri A. Mankelevich[b] and Nikolay V. Suetin[b]

[a] *School of Chemistry, University of Bristol, Bristol, UK BS8 1TS. E-mail: mike.ashfold@bris.ac.uk*
[b] *Nuclear Physics Institute, Moscow State University, 119899 Moscow, Russia*

Received 15th May 2001, Accepted 27th June 2001
First published as an Advance Article on the web 14th August 2001

We describe laser and mass spectroscopic methods, and related modelling studies, that have been used to unravel details of the gas phase chemistry involved in diamond chemical vapour deposition (CVD) using both H/C (*i.e.* hydrocarbon/H_2) and H/C/O (*e.g.* CO_2/CH_4) gas mixtures, and comment on the relative advantages and limitations of the various approaches. In the case of the more extensively studied hydrocarbon/H_2 systems we pay particular emphasis to investigations (both experimental, and 2- and 3-dimensional modelling) of transient species like H atoms and CH_3 radicals, their spatial distributions within the reactor and the ways in which these distributions vary with process conditions, and the insight provided by such investigations into the chemistry underpinning the diamond CVD process. These analyses serve to highlight the rapid thermochemical cycling amongst the various hydrocarbon species in the reactor, such that the gas phase composition in the vicinity of the growing diamond surface is essentially independent of the particular hydrocarbon source gas used. Such applies even to the case of hot filament activated C_2H_2/H_2 gas mixtures, for which we show that CH_3 radical formation (hitherto often presumed to involve heterogeneous hydrogenation steps) can be fully explained in terms of gas phase chemistry. Diamond growth using H/C/O-containing gas mixtures has traditionally been discussed in terms of an empirically derived H–C–O atomic phase composition diagram (P. K. Bachmann, D. Leers, H. Lydtin and D. U. Wiechert, *Diamond Relat. Mater.*, 1991, **1**, 1). Detailed studies of microwave activated CO_2/CH_4 gas mixtures, accompanied by simpler zero-dimensional thermochemical modelling of this and numerous other H/C/O-containing input gas mixtures, provide a consistent rationale for the 'no growth', 'diamond growth' and 'non-diamond growth' regions within the H–C–O atomic phase composition diagram.

I. Introduction

Diamond, the sp^3 bonded allotrope of carbon, has many extreme properties (Table 1) which encourage applications spanning hard, wear resistant coatings (for cutting tools, but also as a protective layer on optical components requiring good IR transparency), free standing IR optics (*e.g.* laser windows, where the unsurpassed room temperature thermal conductivity of diamond can be advantageous also), and thermal management (*e.g.* as a heat sink for small high current laser diodes).[1] The early 1980s saw the first demonstrations of the growth of thin films of polycrystalline diamond by chemical vapour deposition (CVD) methods,[2–4] since which time there has been an explosion of interrelated activities variously aimed at improving our understanding of the underpinning chemical physics of the CVD process and of the factors that influence the film quality, morphology and/or growth rate, and at exploring many of the new application opportunities that arise given that diamond is now available in thin film form.[5]

Table 1 Selected properties of natural diamond (from ref. 1)

Extreme mechanical hardness (~90 GPa)
Strongest known material, highest bulk modulus (1.2×10^{12} N m^{-2})
lowest compressibility (8.3×10^{-13} m^2 N^{-1})
Highest room temperature thermal conductivity (2×10^3 W m^{-1} K^{-1})
Broad optical transparency (deep UV to far IR)
Good electrical insulator (room temperature resistivity ~10^{13} Ω cm)
Wide bad gap (5.4 eV)
Very resistant to chemical corrosion
Biologically compatible
Exhibits low or 'negative' electron affinity

The CVD process involves activation of an appropriate gaseous mixture in the vicinity of a suitably heated substrate upon which polycrystalline diamond will deposit. Most laboratory research to date has centred on hot filament (HF) or low power (a few kW) microwave (MW) plasma enhanced activation, using comparatively simple bench-top reactors and pressures in the range 10–50 Torr, while most industrial production of CVD diamond now involves high power microwave systems or, occasionally, use of direct current (dc) plasma jets. Diamond CVD has been demonstrated also using a combustion (*e.g.* oxy-acetylene) flame, both at atmospheric and reduced pressure; such combustion systems have also been subjected to a variety of mass spectrometric and laser diagnostics[6–8] but generally fall outside the focus of this review. Schematic illustrations of the two main types of reactor used for laboratory based research are shown in Fig. 1. The gas mixture used most commonly consists of small amounts (~1%) of a hydrocarbon (usually methane) in hydrogen, but diamond CVD has been demonstrated using a wide variety of alternative carbon-containing gases. C/H/O-

DOI: 10.1039/b104265n

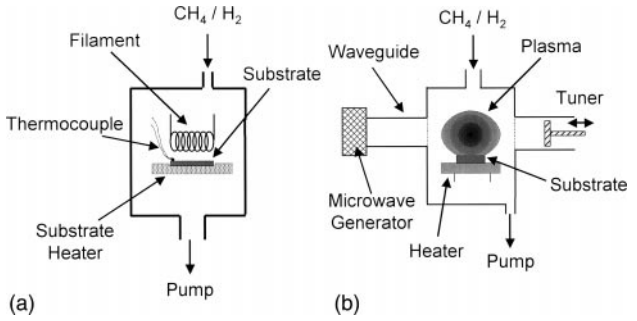

Fig. 1 Schematic illustrations of (a) HF and (b) MW-CVD reactors as used in laboratory studies of diamond CVD.

containing gas mixtures have attracted considerable recent interest,[9–11] while other studies have explored the consequences of trace additions of other gas phase species (*e.g.* B, N, P and Cl-containing precursors), both on the deposition process itself and on the properties of the resulting diamond films. Commonly used substrates for supporting diamond film growth include Si, Mo and W, all of which show the necessary tendency for interfacial carbide formation at the optimum growth temperature ($\sim$800 °C).

Any thorough understanding of diamond CVD requires knowledge of the chemical environment in the vicinity of the diamond film during growth. Thus we need information on factors such as the gas phase species present, the sources, interconversion and sinks of the key reactive (radical) species, their spatial distribution and their transport through the gas, the chemistry occurring at the gas/surface interface, and the way in which all of these factors vary with, for example, temperature, pressure and the extent of activation (*i.e.* filament temperature or applied microwave power). Much of this potential complexity is illustrated schematically in Fig. 2 for the case of a CH_4/H_2 gas mixture. This Article concentrates on experimental and theoretical studies of the gas phase chemical composition in CVD reactors used for diamond growth operating with hydrocarbon/H_2 and with C/H/O-containing gas mixtures and, in particular, upon the various spectroscopic techniques that have been employed to obtain concentration profiles of key reactive species. Results from such studies are considered in the light of companion numerical modelling of low power diamond CVD reactors, and the overall picture reviewed, prior to concluding with a brief consideration of some of the outstanding questions that remain.

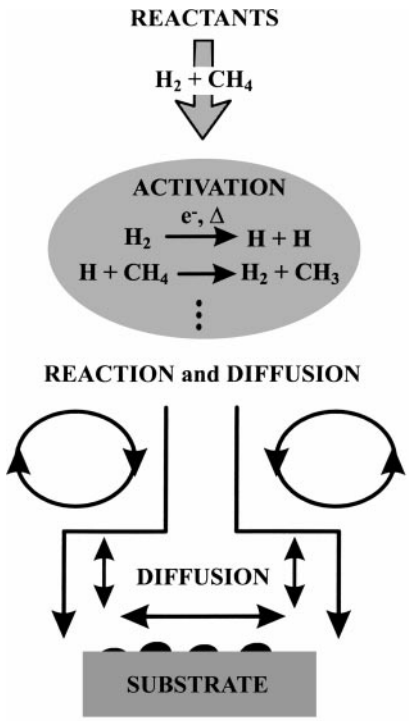

Fig. 2 Schematic illustrating some of the more important physicochemical processes occurring during diamond CVD using a CH_4/H_2 input gas mixture (after ref. 5).

II. Growth from hydrocarbon/H_2 gas mixtures

(a) Stable species: H_2 and hydrocarbons

Hydrocarbon/H_2 mixtures have received extensive investigation, both because of their (apparent) chemical simplicity and because of their compatibility with simple HF-CVD reactors (addition of even trace amounts of O_2 causes rapid destruction of the hot filament). Molecular hydrogen is by far the most abundant gas phase species in such CVD environments though, of course, most of it passes unaltered through the reaction chamber and is exhausted through the pump. H_2—a centrosymmetric diatomic molecule—is Raman but not infrared active. Relevant spectroscopic probing to date has been largely confined to coherent anti-Stokes Raman spectroscopy (CARS). This is a four-wave mixing technique which employs two simultaneous laser pulses, traditionally termed the pump and probe pulses, of respective frequencies ω_1 and ω_2. These interact through the third-order non-linear susceptibility of the medium to generate a coherent CARS signal at frequency $\omega_3 = 2\omega_1 - \omega_2$. The difference $\omega_1 - \omega_2$ is varied by tuning ω_2, thereby achieving resonance with Raman active rovibrational transitions of the target molecule of interest ($\sim$4155 cm^{-1} in the case of H_2). Measurement of two or more such transitions, together with careful calibration experiments, affords sufficient measure of the rovibrational quantum state population distribution to yield a gas temperature (assuming local thermodynamic equilibrium). Since the signal originates from the small volume where the two focused laser beams overlap, CARS has found quite widespread use as a means of determining local gas temperatures and temperature profiles in HF-CVD reactors.[12–15] As with all Raman techniques, the ultimate sensitivity of CARS is rather poor when compared with most of the other laser diagnostic methods discussed later. However, the CARS signal strength scales with the square of the number density of the species of interest; as a result the technique has been used for both temperature and concentration profiling not just of H_2, but also of other of the more abundant gas phase species (notably CH_4 and C_2H_2) in an HF-CVD reactor.[12] Gas temperatures in such a reactor (and their spatial variation) have also been estimated by measuring the relative intensities of individual rovibronic transitions in the $B\,^1\Sigma_u^+$–$X\,^1\Sigma_g^+$ absorption system of H_2 in the vacuum ultraviolet (VUV),[16] while infrared diode laser absorption spectroscopy has also been used to detect C_2H_2, C_2H_4 and CH_3 radicals in such a reactor.[17] Both of these absorption techniques, and the cavity ring down spectroscopy (CRDS) method discussed later, provide column densities (*i.e.* a measurement of all absorbing species along the line of sight) and thus require careful interpretation if, as in most CVD reactors, the temperature and/or species concentrations show an inhomogeneous spatial distribution along the column.

Our group has employed *in situ* molecular beam mass spectrometry (a technique whereby a small fraction of the gas mixture used in diamond CVD is sampled continuously through an orifice located in, or close to, the growing diamond film) to monitor relative concentrations of the various stable hydrocarbon species, and of CH_3 radicals, as a function of the input gas mixture, position and/or process conditions, in both HF and MW-CVD reactors.[18–20] Fig. 3 provides illustrative data sets obtained using three different hydrocarbons, each diluted in H_2 so as to achieve a 1% input

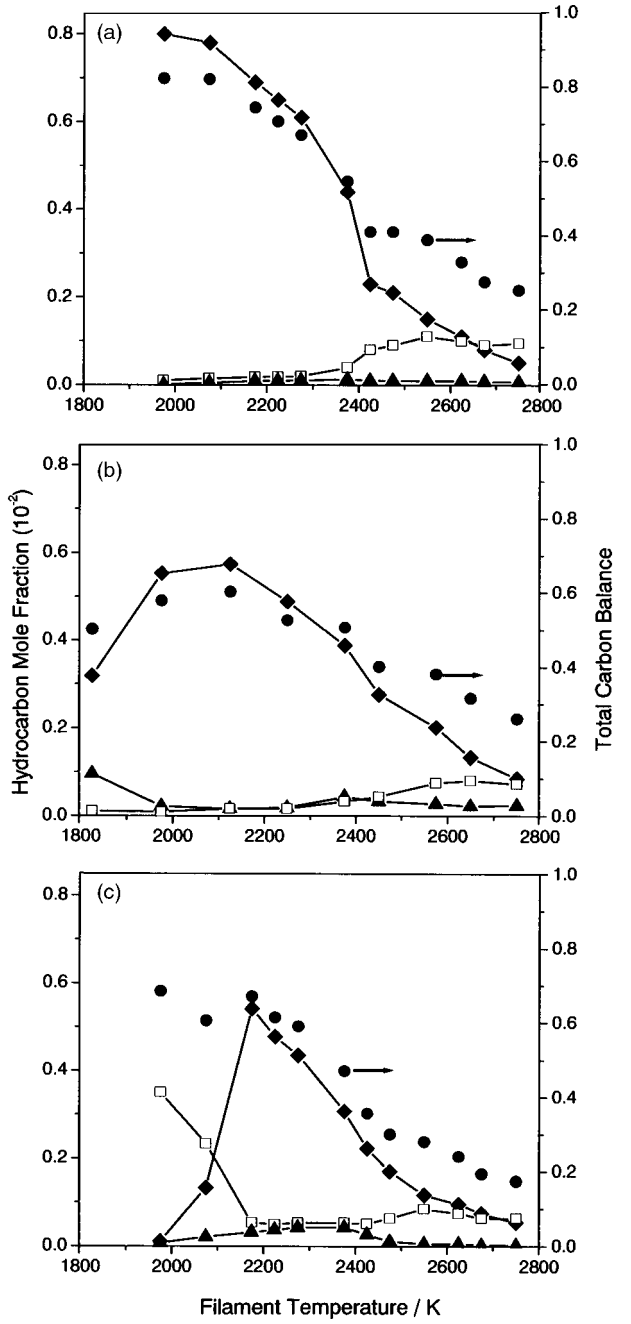

Fig. 3 Mole fractions of CH_4 (◆), C_2H_2 (□) and C_2H_4 (▲) measured by MBMS sampling 6 mm from the filament in an HF-CVD reactor, as a function of T_{fil}, for gas mixtures of (a) 1% CH_4 in H_2, (b) 0.5% C_2H_4 in H_2 and (c) 0.5% C_2H_2 in H_2. In each case, the total gas flow rate was 100 sccm and the pressure 20 Torr. The measured carbon balance (●) is observed to fall with increasing T_{fil}. This is attributable to the Soret effect, whereby heavier species diffuse preferentially from the hottest regions of the gas (adapted from ref. 21).

mole fraction of carbon, as a function of filament temperature, T_{fil}, in an HF-CVD reactor. One striking result emerged from these,[21] and other of the earlier studies;[22,23] namely, that the gas phase composition in the vicinity of the filament at temperatures appropriate for optimal diamond CVD ($T_{fil} \sim$ 2400 °C) is essentially independent of the carbon source gas. Fig. 3(a) shows increasing T_{fil} causing a progressive conversion of CH_4 to C_2H_2 near the filament in the case of a CH_4/H_2 input gas mixture; the steady state concentrations of C_2H_4 and C_2H_6 are low in comparison. Fig. 3(b) and (c) show analogous data for C_2H_4/H_2 and C_2H_2/H_2 gas mixtures. In both cases, significant conversion of the C_2 hydrocarbon to CH_4 is observed at relatively low T_{fil}, followed by CH_4 to C_2H_2 conversion as T_{fil} is increased.

Such trends are broadly consistent with expectations based on simple equilibrium thermodynamics. Given the thermodynamic data in Table 2, we could predict that the Gibbs energy for the overall conversion (1) will change sign from positive to negative (*i.e.* the equilibrium will start to favour products rather than reactants) at gas temperatures T_{gas} above ~1700 K.

$$2CH_4 \rightleftharpoons C_2H_2 + 3H_2 \quad (1)$$

Fig. 4 shows the results of a more elaborate calculation of the way in which the equilibrium composition of a mixture of 1% CH_4 in H_2, at 20 Torr pressure, evolves with temperature over the range 1000–2500 K. This calculation uses literature values for the temperature dependent rate constants for elementary gas phase reactions involving H, H_2 and all C_xH_y ($x \leqslant 2$, $y \leqslant 6$) species.[24] Of course, this analysis still grossly oversimplifies the real situation prevailing during diamond CVD. The gas mixture is not static, but flowing through a

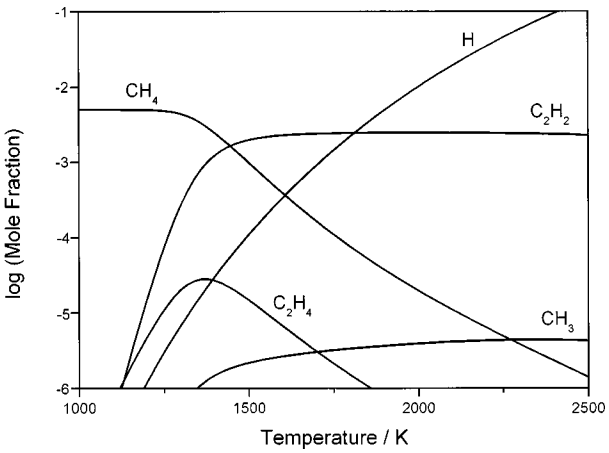

Fig. 4 Homogeneous equilibrium mole fractions for different gas temperatures assuming an input gas mixture comprising 1% CH_4 in H_2 at a pressure of 20 Torr, calculated using the relevant forward and backward rate constants (from ref. 24) and propagating to long time.

Table 2 Thermodynamic data for selected stable species involved in diamond CVD, at room temperature, 1200 and 2000 K (from ref. 90)

	$\Delta_f H°$/kJ mol^{-1}			$\Delta_f G°$/kJ mol^{-1}			$S°$/J K^{-1} mol^{-1}		
Species	298 K	1200 K	2000 K	298 K	1200 K	2000 K	298 K	1200 K	2000 K
H_2	0	0	0	0	0	0	130.7	171.8	185.4
CH_4	−74.9	−91.4	−92.7	−50.7	41.5	130.8	186.3	261.3	305.9
C_2H_2	226.7	222.7	219.9	209.2	158.9	117.2	200.9	282.0	321.3
O_2	0	0	0	0	0	0	205.1	250.0	268.7
CO	−110.5	−113.2	−118.9	−137.2	−217.8	−286.0	197.7	240.7	258.7
CO_2	−393.5	−395.1	−396.8	−394.4	−396.1	−396.3	213.8	279.4	309.3
H_2O	−241.8	−249.0	−251.6	−228.6	−181.4	−135.5	188.8	240.5	264.8

reactor in which there are large temperature gradients. The equilibrium (1) will be shifted towards the right hand side (*i.e.* C_2H_2) in the vicinity of the hot filament, whereas CH_4 should dominate in cooler regions (*i.e.* the reactor walls). These 'hot' and 'cool' regions are, at most, only a few cm apart in a typical laboratory based CVD reactor, so the species of interest will diffuse through the interaction zone in a time of the order of a second or less. This finite residence time prevents the gas mixture from attaining true chemical equilibrium; so much so, in fact, that an analogous calculation starting from a C_2H_2/H_2 gas mixture predicts insignificant conversion to CH_4—in contrast to experimental observation (Fig. 3(c)). Additionally, as discussed more fully below, the H atom concentration throughout most of the volume of the reactor is far in excess of that predicted on the basis of equilibrium thermodynamics. Clearly, therefore, any detailed description of the gas phase processes underpinning diamond CVD must take due account of the temperature and concentration gradients, and species and heat transport, within the reactor. Sample results based on such 3-D numerical simulations are presented at the end of this section.

(b) Transient species

H atoms and CH_3 radicals are now recognised as key constituents in most diamond CVD environments. This section considers various spectroscopic techniques that have been applied to monitoring such radicals in CVD reactors, and the overall picture that emerges from such studies.

H atoms. The concentration of atomic H in the vicinity of the growing diamond surface is a critical factor determining film quality and growth rates. H atoms initiate most of the gas phase chemistry in low power CVD reactors. They continuously create (by abstraction of surface terminating hydrogen atoms) and re-terminate (thereby preventing the reconstruction to non-diamond forms) the reactive surface sites necessary for the propagation of the diamond lattice. H atoms also preferentially etch deposited non-diamond carbon,[25–29] and their recombination on the growing diamond surface can make a significant contribution to the substrate heating.[30,31]

Balmer series emission is a major component of the visible radiation emanating from most plasma activated H_2/CH_4 gas mixtures, but the electronically excited H atoms (with $n \geqslant 3$) responsible for this spontaneous emission constitute only a very small (spatially and process condition dependent) fraction of the total H atom number density. Fig. 5 summarises some of the optical techniques that have been used for profiling the concentration of *ground*-state H atoms—the key quantity of interest—in diamond CVD reactors. These include direct absorption on the $n = 2 \leftarrow n = 1$ Lyman-α transition,[32] laser induced fluorescence (LIF) measurements—monitoring, for example, $n = 3 \rightarrow n = 2$ Balmer-α emission following $n = 3 \leftarrow n = 1$ two-photon excitation[33–36] or $n = 4 \rightarrow n = 2$ Balmer-β emission following three-photon excitation of the $n = 4 \leftarrow n = 1$ transition,[7] multiphoton ionisation using 364.6 nm photons, resonance enhanced at the three photon energy by the $n = 2$ state (a so-called 3 + 1 REMPI process),[37] and *in situ* third harmonic generation (THG).[14,38] THG is a process in which three identical exciting photons (with frequency ω) interact through the third-order non-linear susceptibility of the medium to generate a coherent beam at frequency 3ω. If (as is usually the case) a focused laser beam is used, the THG process exhibits rather exacting phase matching requirements such that 3ω radiation is produced only on the high frequency side of strongly allowed one-photon absorptions (*e.g.* the H Lyman-α absorption at 121.6 nm). Its potential as a gas phase diagnostic[39] stems from the fact that the frequency shift between the peak of the strong one photon absorption and the peak of the excitation function for forming 3ω radiation is

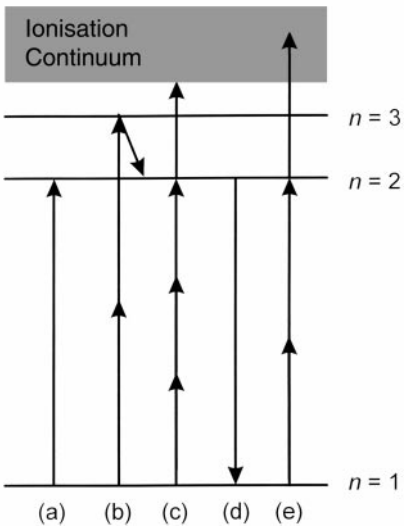

Fig. 5 Energy level diagrams depicting various of the laser based techniques used for H atom detection in diamond CVD environments: (a) direct absorption at 121.6 nm, (b) two-photon absorption to the $n = 3$ state with observation of the resulting laser induced fluorescence, (c) 3 + 1 REMPI *via* the $n = 2$ state, with possible THG (d) and (e) 2 + 1 REMPI *via* the $n = 2$ state.

directly proportional to the number density of the absorber of interest (H atoms in the present case). All four methods have their virtues, but also their attendant limitations. For example, monitoring H atom concentrations in absorption requires the availability of tuneable radiation at 121.6 nm—a wavelength deep in the VUV region that, in studies of diamond CVD to date, has been provided by a synchrotron source.[32,40] The large oscillator strength of the Lyman-α transition means that most growth environments will be optically 'thick' at this wavelength—*i.e.* the standard Beer–Lambert relation linking absorbance and concentration will not be obeyed—thus hampering estimation of the H atom column density. By way of further complication, Childs *et al.*[40] have reported the presence of an overlapping C_2H_2 absorption feature at 121.6 nm, and near-resonant absorption due to rovibrationally excited H_2. All of these absorptions must also be a concern in H atom concentration estimates derived from THG measurements, since they will affect both the local bulk refractive index (and thus both the efficiency and the wavelength dependence of the THG process) and the transmission of any THG radiation from the region probed by the laser to the detector. H atom concentration estimates derived from 3 + 1 REMPI measurements *via* the $n = 2$ state must also be viewed with some caution because of the contributions from (off-resonant) THG that can occur at the pressures (tens of Torr) used in most diamond CVD environments.

We, and others, have chosen to focus on H atom detection methods involving *two*-photon resonant excitation. As with the three-photon processes summarised above, these involve use of a focused pulsed laser and thus offer the prospect of 3-D spatial resolution (<1 mm in diameter and a few mm in length, defined by the laser focal volume). Two choices merit consideration. The more widely used is two-photon laser induced fluorescence (sometimes given the acronym TALIF).[34,41] Given available laser technology, $n = 3 \leftarrow n = 1$ two photon excitation at 205.1 nm, with subsequent detection of the Balmer-α emission at 656.1 nm, is the only practical detection scheme, but its implementation is complicated by the need to separate the fluorescence (spatially and/or temporally) from the intense luminous background from the HF or the plasma ball that is inevitably present in most CVD reactors. Use of this short excitation wavelength also introduces the possibility of unintentional photochemical pro-

duction of H atoms following absorption of probe laser radiation by various of the hydrocarbon species (*e.g.* C_2H_2 and CH_3) present in the growth mixture. TALIF is subject to collisional quenching,[33,36] so careful calibration experiments are required prior to the extraction of absolute atom number densities. Fig. 5 also illustrates the fact that, at the laser intensities necessary to cause significant coherent two-photon excitation of a detectable number of H atoms to the emitting $n = 3$ state, some fraction of these excited atoms must inevitably absorb one further photon and be ionised. This represents another possible loss process for population in the $n = 3$ state, and should be borne in mind when attempting to relate measured TALIF intensities to H atom number densities in the probe volume. We chose to investigate and validate H atom detection by REMPI at the longer excitation wavelength of 243.1 nm, resonant at the two photon energy with the $n = 2 \leftarrow n = 1$ transition, where unintended photochemistry of molecular species present in the gas mixture is much less probable.

Our experimental set-up and procedure has been described elsewhere.[42] The HF-CVD reactor comprises a six-way cross incorporating a fixed REMPI probe. Two side ports allow entry and exit of the probe laser beam, while a third (in the same horizontal plane) provides an observation window through which the HF is viewed by a two-colour optical pyrometer. The HF and (if required) the substrate holder are attached to a common cradle suspended from a linear translation stage. The whole cradle can be translated vertically by $\leqslant 25$ mm relative to the fixed laser focus and REMPI probe, thereby enabling spatially resolved profiling of key species. The coiled filament is oriented with its long axis parallel to the direction of laser propagation. The chamber is evacuable to a base pressure of $\sim 10^{-2}$ Torr. Typical growth runs would employ 0.5 or 1% CH_4 in H_2. These gases are metered by mass flow controllers, pre-mixed in a manifold and fed into the reactor through a port located above the cradle assembly, so as to maintain the total flow (100 sccm) and chamber pressure (20 Torr). H atoms are detected by 2 + 1 REMPI using 243.1 nm radiation generated by a Nd-YAG pumped frequency doubled dye laser.

H^+ ions formed by REMPI in the focal volume are collected on a negatively biased probe wire, the tip of which is positioned ~ 2 mm from the laser focus. A filter and accompanying power supply prevent the probe bias voltage (and thus possibly the collection efficiency) changing as the HF (and the inevitable cloud of thermionic emission that accompanies it) is translated, whilst passing the transient REMPI current. Translating the filament enables spatially resolved measurements whilst maintaining the laser focal volume and collection probe fixed. Fig. 6(a) shows illustrative spectra of the $2s \leftarrow 1s$ two-photon transition of atomic H obtained by monitoring the total H^+ ion signal reaching the probe, as the excitation frequency was scanned. For these two spectra the probe laser was focused at a distance $d = 0$ and 10 mm, respectively, from the centre of the lower edge of the HF, the input gas was pure H_2, and the substrate and its holder were not present in the chamber. Each data point is the summation of ten laser shots and has been power normalised against the square of the measured UV light intensity. Analysis of such lineshapes can provide a measure of the d dependence of the local gas temperature, T_{gas}, and of the relative H atom number density in the focal volume. The solid curves through the data points are the results of a least squares fit to a Gaussian lineshape function. The bandwidth of the frequency doubled probe laser makes minimal contribution to the measured linewidth and, after deconvoluting this contribution, the remaining linewidth can be attributed to Doppler broadening. $\Delta\nu_D$, the full width half maximum (FWHM) of such Doppler

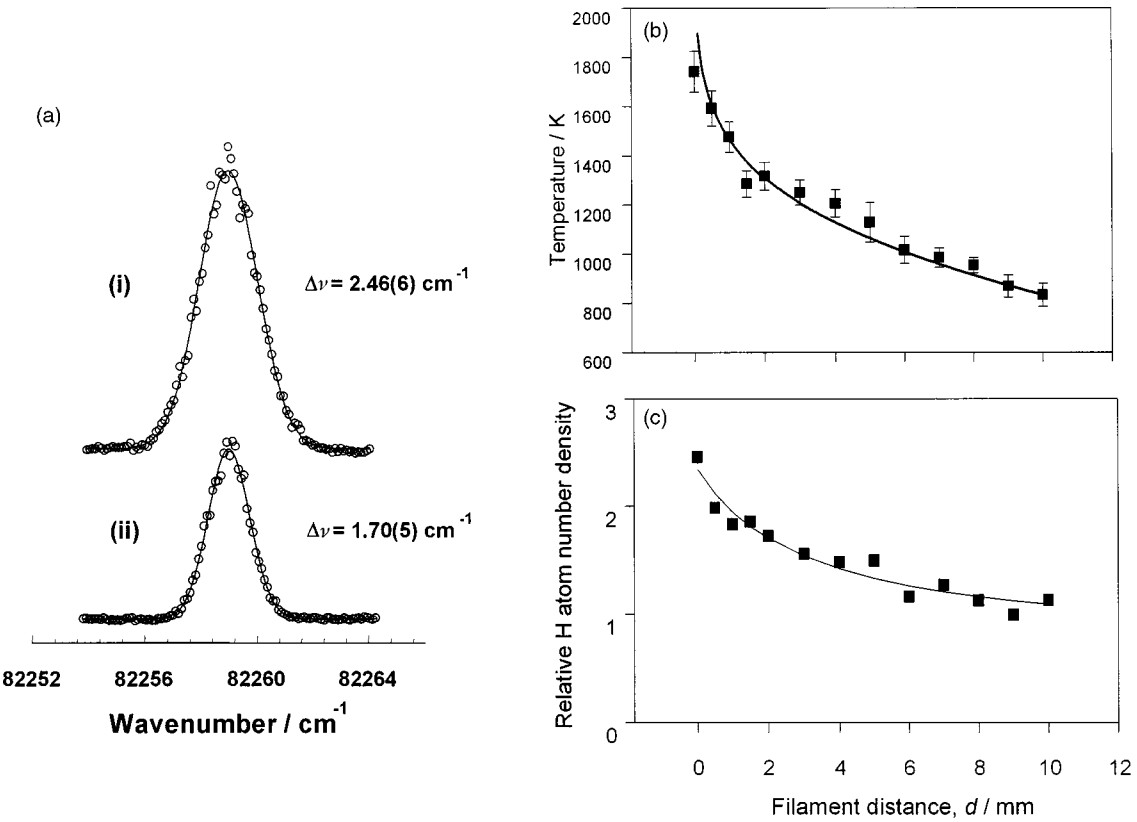

Fig. 6 (a) Lineshapes of the H atom $2s \leftarrow 1s$ two-photon transition recorded using pure H_2 (pressure: 20 Torr, flow rate: 100 sccm) at $d = 0$ (i) and 10 mm (ii) from a Ta filament held at $T_{fil} = 2375$ K. The solid curve in each case is a least squares fit to a Gaussian function, the FWHM of which (after deconvoluting the laser linewidth) provides a measure of the local temperature, T_{gas}, while the respective areas under such lineshapes provide a measure of the relative H atom number density, [H]. Analysis of many such lineshapes, recorded at different d, enable derivation of the radial dependences of T_{gas} and [H] shown in (b) and (c). The solid curve in (b) is obtained using eqn. (3) with $R_f = 125$ μm.

broadened lineshapes, is related to the local translational temperature, T_{gas}, *via*

$$\Delta\nu_D = \frac{\nu_0}{c}\sqrt{\frac{8kT_{gas}\ln 2}{M}}, \quad (2)$$

where ν_0 is the line centre transition frequency, c is the speed of light and M is the mass in kg. Since the individual lineshapes are correctly power normalised, the respective areas under the fitted Gaussians are proportional to the *relative* H atom number density, [H], in the focal volume. Determining *absolute* number densities is much harder, given the inevitable uncertainties in defining the extent of the focal volume.

Fig. 6(b) and (c) show the deduced d dependences of, respectively, T_{gas} and [H] in a sample of 20 Torr pure H_2 (100 sccm flow rate) and $T_{fil} = 2360$ K. No change in either quantity is discerned upon reducing the H_2 flow rate to 50 sccm, thus encouraging the view that diffusion is the dominant transport mechanism in low pressure (*e.g.* HF-CVD) reactors.[43–46] The solid curve through the data points in Fig. 6(b) is obtained using the model expression[47]

$$T_d = T_{d=0}\{1 - [1 - (T_L/T_{d=0})^2]\ln((d + R_f)/R_f)/\ln(L/R_f)\}^{0.5}, \quad (3)$$

where $T_{d=0}$ and T_L are the gas temperature in the immediate vicinity of, and at a distance L from, the HF, and R_f is the filament radius. The good match between experiment and eqn. (3), which has been used to model the radial gas temperature profiles in other axially symmetric HF-CVD reactors also,[13,34] serves to validate both the reactor modelling[47] discussed more fully below, and the use of H atom Doppler lineshape analysis as a rather straightforward alternative to CARS for probing spatially localised gas temperatures in a HF-CVD reactor. Similar [H] *vs.* d trends in HF-CVD reactors have been derived *via* VUV absorption,[40] TALIF[33] and THG[14] probing, and deduced using the recombination enthalpy technique.[48] All support the view that H atoms in HF-CVD reactors are formed at the filament surface, and diffuse into the bulk. The H atom recombination rate at typical reactor pressures and temperatures is so slow that, throughout most of the reactor including, most importantly, close to the substrate surface, the H atom concentration is far in excess of that expected on the basis of equilibrium thermodynamics.

Having established the diagnostic method, it is possible to explore the way [H] varies with different process parameters. Thus, for example, the H atom signal measured at any given T_{fil} and d is found to be essentially independent of $p(H_2)$, the H_2 pressure.[42] TALIF studies,[33,34] and measurements of the pressure dependence of the power consumption by hot Ta and W filaments when used to dissociate H_2,[46] have reached similar conclusions. Such findings support the view that, at the prevailing gas pressures and temperatures, H atoms arise as a result of H_2 bond fission on the surface of the hot filament and therefore exhibit kinetics that are zero order with respect to $p(H_2)$. A gradual decrease in [H] observed at higher $p(H_2)$ is attributable to the three-body homogeneous recombination process

$$H + H + M(H_2) \rightarrow H_2 + M(H_2). \quad (4)$$

Fig. 7 shows the ways in which T_{gas} and [H] near the HF vary as T_{fil} is increased. T_{gas} is found to scale almost linearly with T_{fil} but, even 1 mm from the HF, is ~700 K cooler than the filament surface. Temperature discontinuities of this magnitude are consistent with findings reported in the early work of Langmuir.[49] The measured H atom number density increases almost exponentially in the temperature range investigated.[42] Plotting ln[H] against $1/T_{fil}$ (a van't Hoff type plot) yields a straight line, the gradient of which we interpret in terms of $-\Delta_{diss}H/R$, where $\Delta_{diss}H$ (240 ± 20 kJ mol^{-1}) is the deduced enthalpy for forming a mole of H atoms on the surface of the HF. This formation process is pictured in terms of reversible elementary steps like

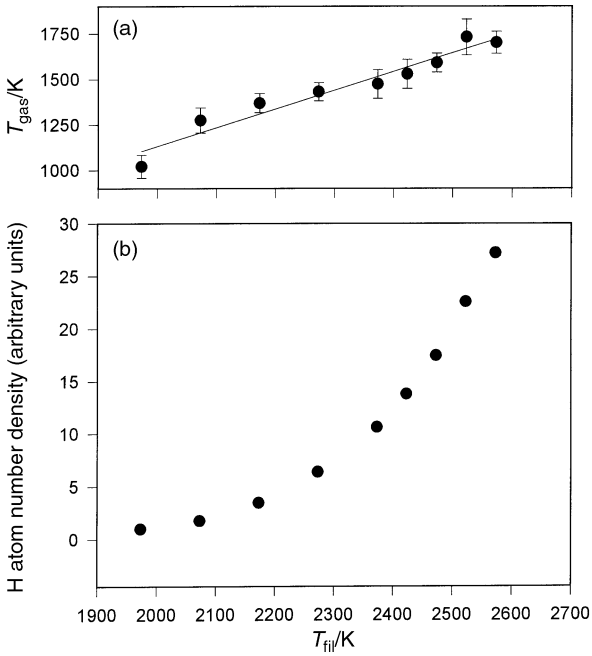

Fig. 7 (a) T_{gas} and (b) relative H atom number densities deduced from analysis of the 2s ← 1s two-photon Doppler lineshapes measured at $d = 1$ mm, plotted as a function of T_{fil}.

$$H_2 + S^* \rightleftharpoons H + SH \quad (5)$$

$$SH \rightleftharpoons H + S^*. \quad (6)$$

Reactions (5) and (−5) describe dissociative adsorption of H_2 on an active site (S*) on the HF surface and H atom recombination on a hydrogen-terminated surface site, respectively, while reactions (6) and (−6) represent desorption and adsorption of an H atom. Increasing T_{fil} will influence the local H atom number density by its effect on all backward and forward reaction rates—not just by helping to surmount any energy barriers associated with these various processes, but also by affecting the mean lifetime of any chemisorbed species on the HF surface, the balance between non-dissociative (not shown) and dissociative adsorption (5), the fraction of surface sites that are 'active' (*i.e.* S* *vs.* SH), and the local gas phase [H]—which affects the extent of contributions from reaction (6). Nevertheless, the sum of these two reactions is simply

$$H_2 \rightleftharpoons 2H, \quad (7)$$

and the similarity between the experimentally deduced $\Delta_{diss}H$ value and that using the tabulated temperature dependence of the equilibrium constant for the purely gas phase version of reaction (7)[50] encourages the view that the main role of the HF surface is to provide an efficient means by which H_2 molecules can attain T_{fil}.

For simplicity, the data shown in Fig. 6 and 7 were obtained using pure H_2, rather than the dilute hydrocarbon/H_2 mixtures required for diamond growth. Addition of CH_4 to the feed-stock gas used in an HF-CVD reactor leads to carburisation of the filament and complicates the problem by introducing a wider range of possible surface sites—the reactivity and stability of each of which will exhibit their own characteristic temperature dependence—and offers a new and efficient reactive loss mechanism for H atoms. Small CH_4 additions cause some reduction in [H] at any given T_{fil}; this becomes more dramatic if some critical hydrocarbon fraction is exceeded.[37,51,52] Both observations are con-

sistent with progressive loss of 'active' sites on the HF surface as the extent of carburisation increases, exacerbated by the conversion of H atoms to H_2 molecules *via* gas phase abstraction reactions like

$$H + CH_4 \rightleftharpoons H_2 + CH_3 . \quad (8)$$

Our discussion to date has concentrated largely on HF-CVD reactors, since these are most amenable to detailed, spatially resolved probing by laser techniques like REMPI or TALIF. In contrast, there have been few comparable studies of MW-CVD reactors: use of REMPI detection methods in such environments is compromised by the steady state concentration of ions in the plasma, while TALIF detection is complicated by the high luminosity of the plasma ball. Lacking the heterogeneous H atom production route afforded by the HF surface, H atom production in a MW-CVD reactor is generally assumed to proceed *via* vibrational excitation and dissociation of H atoms by a succession of electron impacts in the plasma,[5] but careful spatially resolved measurements of T_{gas} and [H] throughout the plasma ball in a MW-CVD reactor remain rare.[53]

Carbon-containing radicals. *In situ* molecular beam mass spectroscopy studies[18–20] of diamond CVD using typically 1% CH_4 in H_2 process gas mixtures, both in HF (Fig. 3) and MW-CVD reactors, have provided clear evidence for substantial conversion of CH_4 to C_2H_2, with ethene (C_2H_4) detectable, but at substantially lower concentration. These studies also show the mole fractions of CH_4 and C_2H_2 under 'standard' growth conditions to be essentially independent of the choice of carbon precursor. Other C-containing species monitored in such reactors include C atoms themselves, by VUV absorption,[40] as well as C_2 and CH radicals by, for example, their spontaneous emission, by direct absorption[54,55] and by laser induced fluorescence. The CH_3 radical is the dominant carbon-containing radical species in such environments, however, appearing with a mole fraction a few percent of that of CH_4 under standard growth conditions. Unlike H atoms and these simple diatomic carbon species, optical emission is not a viable route to detecting CH_3 radicals; all known excited electronic states of CH_3 predissociate too fast for radiative decay to be a competitive population loss process. Spectroscopic techniques that have been applied to CH_3 radical detection during diamond CVD include direct absorption spectroscopy, in the infrared,[56] UV[32,54,57] and vacuum UV,[40] 2 + 1 REMPI spectroscopy[15,58–62] and cavity ring down spectroscopy (CRDS).[63–65]

CRDS[66,67] offers a possible route to absolute column densities with high sensitivity and reasonable spatial resolution. It involves measurement of the time decay of a light pulse injected into an optical cavity which, in the examples reported thus far, is an HF-CVD reactor operating with CH_4/H_2 gas mixtures, bounded by two mirrors exhibiting high (>99%) reflectivity at the chosen probe wavelength, 213.9 nm, within the $\tilde{B}$–$\tilde{X}$ electronic transition of the CH_3 radical. In the absence of any absorbers, the light within this cavity should decay exponentially with a time constant, the so-called ring-down time, determined by the mirror reflectivities and the cavity length. The presence of an absorbing sample increases the cavity losses and results in a reduced ring down time which, provided the absorption follows the Beer–Lambert law, can be related to the sample absorbance. Given a value for the absorption coefficient of the CH_3 radical at 213.9 nm (which was assumed to be temperature dependent), and making an educated guess as to the absorption length over which they are likely to be present in a HF-CVD reactor (approximated as the length of the hot filament), Zare and co-workers were able to estimate methyl[63–65] and CH[55] radical number densities, along the column parallel to the HF axis, as a function of the radial distance d from the filament, and as a function of both T_{fil} and the substrate temperature. [CH_3] was deduced to peak at a distance ~4 mm from the HF, in contrast to the H atom radial dependence (Fig. 6(c)). This, at the time, somewhat unexpected result was rationalised by 3-D simulations of the Stanford HF-CVD reactor that included heat and mass transport, diffusion, the detailed gas phase reaction mechanisms, H atom production at the filament, and gas–surface chemistry at the substrate.[68] These simulations confirmed H atom abstraction from CH_4 as the principal route for forming CH_3 radicals, and showed the CH_3 production rate and, consequently, the CH_3 mole fraction, $X(CH_3)$ to both be maximal at $d \sim 0$. That the number density, [CH_3], is observed to show a local minimum at $d \sim 0$ reflects the rapid fall in T_{gas} (and thus the rapid increase in total gas concentration) with increasing d, compounded by the effects of mass dependent thermal diffusion (the Soret effect), which ensures a relative deficiency of heavier species (*i.e.* all species other than H or H_2) near the HF.[18–20]

CRDS has its limitations, however. It provides a 2-D spatial profile, since target species anywhere along the viewing column will contribute to the measured signal. Number density estimates deriving from measured ring down times will be sensitive to any temperature dependence of the absorption cross-section at the probe wavelength, and also require some assumptions about the way in which the number density varies along the viewing column. Furthermore, for the specific case of CH_3 radical detection in a HF-CVD reactor operating with a hydrocarbon/H_2 feed-stock gas, analysis may be complicated further by the fact that C_2H_2 molecules, which build up in the vicinity of the HF (recall Fig. 3), show significant hot band absorption at wavelengths ~215 nm used when probing CH_3 radicals *via* their $\tilde{B}$–$\tilde{X}$ system. Thus we,[61,62] and others,[15,58–60] have investigated the use of 2 + 1 REMPI for probing CH_3 radicals.

Fig. 8(a) shows a power normalised spectrum of the $3p_z;{}^2A_2''$–$\tilde{X}\,{}^2A_2''$ origin band transition of the CH_3 radical obtained using a 1% CH_4/H_2 gas mixture in the same HF-CVD reactor as used for the H atom studies described previously, with $T_{fil} = 2475$ K, probing at $d = 4$ mm. The Q branch dominates the spectrum, with weak underlying O, P, R and S branch structure contributing to the underlying pedestal.[60,62] The simulation shown above the experimental spectrum relies on prior knowledge of the appropriate ground and excited state spectroscopic constants, two-photon rotational linestrengths, and excited state predissociation behaviour; knowing these parameters,[62] the only adjustable parameter needed to model the band contour is the rotational temperature, T_{rot}. The best-fit simulation of the spectrum shown in Fig. 8(a) requires $T_{rot} = 1150$ K. Reference to Fig. 6(b) shows this value to be in very good agreement with the gas temperature derived from H atom Doppler lineshape analysis (for the same T_{fil} and d). Such accord is not unexpected, since the collision frequency at typical temperatures and pressures prevailing in HF-CVD reactors is ~10^8 s^{-1}; it serves to validate the concept of local thermodynamic equilibrium (LTE) that is normally assumed in discussion of such reactors.

Thus we conclude that 2 + 1 REMPI is a viable means of monitoring CH_3 number densities in an HF-CVD reactor, and proceed to explore the way in which [CH_3] varies as a function of d, and of process conditions like T_{fil}, the hydrocarbon source gas, and the hydrocarbon/H_2 mixing ratio. The simplest experimental measurable, however, is a power normalised REMPI signal at a single probe wavelength within the $CH_3(3p_z;{}^2A_2''$–$\tilde{X}\,{}^2A_2'')$ transition, rather than the entire band contour. Converting such a measurement into the required relative number densities requires knowledge of T_{gas}, as a function of d (Fig. 6(b)), and correction factors to allow for the fact that both the origin band contour and the fraction of the total CH_3 population that is in the probed $v = 0$ level

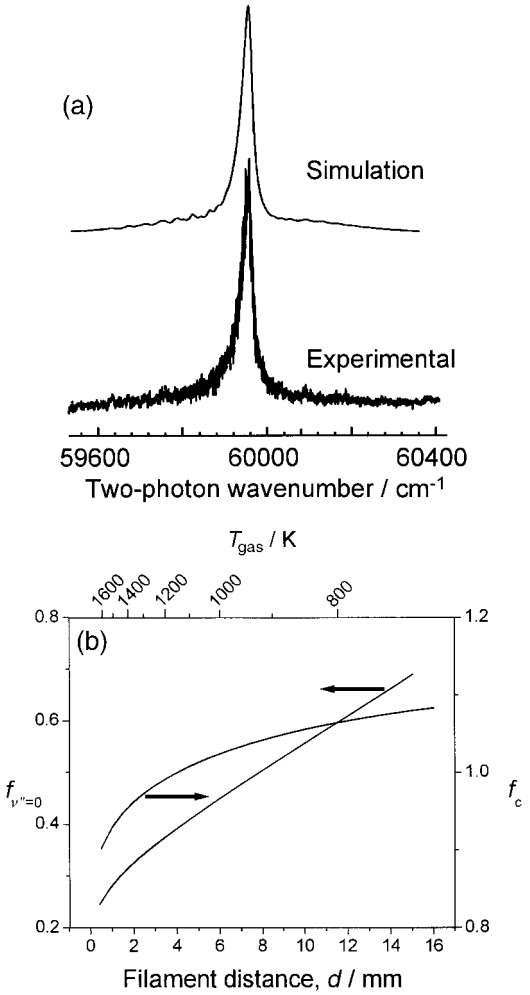

Fig. 8 (a) $2+1$ REMPI spectrum of the $CH_3(3p_z;{}^2A_2'' \leftarrow \tilde{X}\,{}^2A_2'')$ transition obtained using a 1% CH_4 in H_2 gas mixture, $T_{fil} = 2475$ K and probing at $d = 4$ mm together with (above) a best-fit simulation of the origin band contour, using spectroscopic parameters listed in ref. 62 and $T_{gas} = 1150$ K. (b) Plot illustrating the variation of the correction factors f_c and $f_{v''=0}$ with T_{gas} and thus, *via* Fig. 6, *d*.

depend on T_{gas}.[60,61] Fig. 8(b) summarises the two temperature dependent factors by which the REMPI signal measured must be divided in order to convert measured signals into relative number densities.[61] f_C is obtained by calculating the $CH_3(3p_z;{}^2A_2''$–$\tilde{X}\,{}^2A_2'')$ origin band contour for several different rotational temperatures in the range $600 \leqslant T_{gas}/K \leqslant 1700$ and then determining the fraction of the total excitation profile which falls within the bandwidth of the probe laser (assumed Gaussian, and centred at a two photon energy of 59 950 cm^{-1}). The other term, $f_{v''=0}$, allows for the fact that the REMPI probe wavelength only samples that fraction of the total CH_3 radical population that is in the ground vibrational state; its temperature dependence is readily calculable given the CH_3 normal mode frequencies and the assumption of LTE.

Three illustrative sets of results are shown in Fig. 9. The first (Fig. 9(a)) shows the measured radial dependence of the CH_3 REMPI signal measured for a 1% CH_4 in H_2 gas mixture and $T_{fil} = 2475$ K, along with the *d* dependence of the CH_3 radical number density, $[CH_3]$, that can be deduced by scaling the measured REMPI signals with the temperature dependent sensitivity factors f_C and $f_{v=0}$. The variation in measured REMPI signal, which peaks at $d \sim 4$ mm, is very reminiscent of that reported in the CRDS studies of CH_3 radicals in an HF-CVD reactor;[63–65] application of the appropriate sensitivity factors leads to a much flatter *d* dependence of $[CH_3]$ near the filament. Fig. 9(b) illustrates the way in

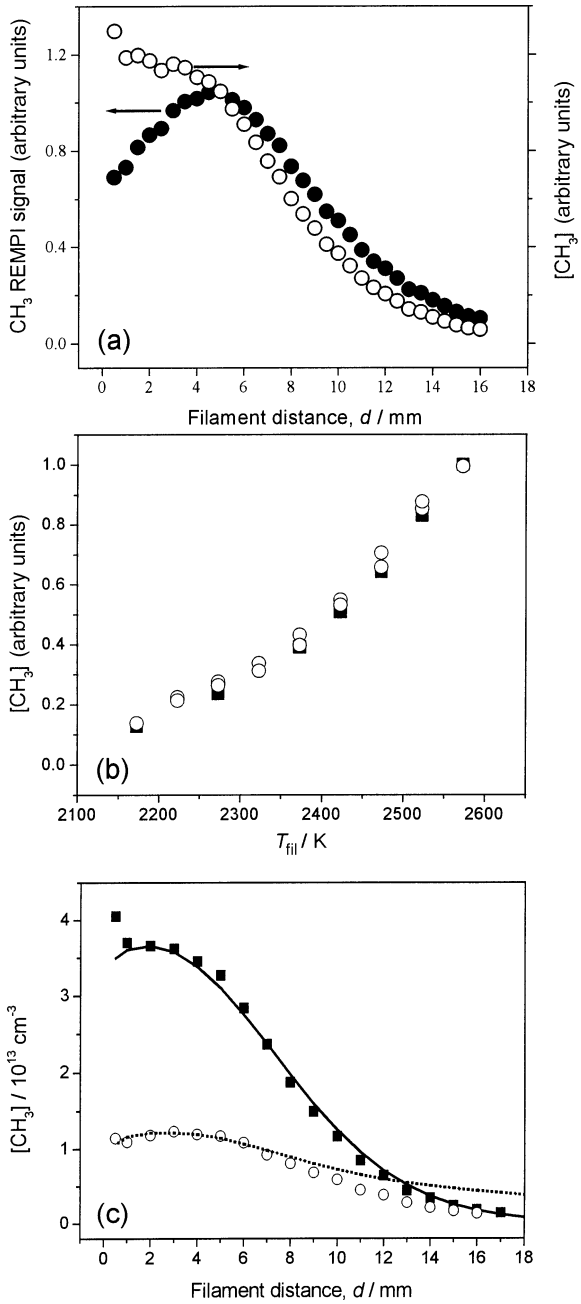

Fig. 9 (a) CH_3 REMPI signal measured for a 1% CH_4 in H_2 gas mixture and $T_{fil} = 2475$ K (●), and the variation of $[CH_3]$ deduced by scaling these REMPI signals with the temperature dependent sensitivity factors f_c and $f_{v''=0}$ (○), both plotted as a function of *d*. (b) Plot highlighting the similar trend of increasing $[CH_3]$ with T_{fil} using 1% CH_4 in H_2 (■) and 0.5% C_2H_2 in H_2 (○) gas mixtures, probing at $d = 4$ mm. The two data sets have been re-scaled vertically to coincide at $T_{fil} = 2575$ K. (c) Experimentally measured *d* dependent $[CH_3]$ profiles obtained using 1% CH_4 in H_2 (■) and 0.5% C_2H_2 in H_2 (○) gas mixtures, with $T_{fil} = 2475$ K. In order to establish a common vertical scale for this plot, measurements were made while switching from CH_4 to C_2H_2 and back, while maintaining T_{fil} and a constant H_2 flow rate. The forms of these relative number density measurements are well reproduced by the results of 3-D simulations (solid and dashed curve, respectively) which assume an H atom production rate, $Q = 6 \times 10^{18}$ cm^{-2} s^{-1} and a near-filament gas temperature $T_{nf} = 2000$ K and, implicitly, yield the absolute number densities shown on the left hand axis.

which $[CH_3]$, measured at $d = 4$ mm, using 1% CH_4 in H_2 and 0.5% C_2H_2 in H_2 gas mixtures, increases with T_{fil}, while Fig. 9(c) compares the deduced radial dependent $[CH_3]$ profiles for 1% CH_4 in H_2 and 0.5% C_2H_2 in H_2 gas mixtures at $T_{fil} = 2475$ K. Clearly, the trend (though not the absolute magnitude) of increasing $[CH_3]$ near the HF with increasing

T_{fil} is the same for both hydrocarbon source gases, as is the general form of the radial dependent $[CH_3]$ profile from each process gas mixture. Toyoda *et al.*[32] suggested a possible gas phase route (involving successive reactions with H atoms and H_2 molecules) for converting C_2H_2 to C_2H_5 radicals, and thence to CH_3 radicals, but were ultimately unable to distinguish between such a gas phase mechanism and a filament surface catalysed route to CH_3 radical formation. Given that all of the simpler kinetic simulations of C_2H_2/H_2 gas mixtures maintained at $T_{gas} \sim 1500$–2000 K for the short residence times appropriate for traditional HF-CVD reactors suggest little conversion to C_1 species, subsequent authors have tended to attribute the observed CH_4 and CH_3 densities to heterogeneous processes occurring on the reactor walls or the growing diamond surface.[5,15] Such seems unlikely, however, given the striking similarities between the C_2H_2/H_2 and CH_4/H_2 data evident in Fig. 9, and the fact that the latter is readily explicable solely in terms of gas phase chemistry.

Modelling C_2H_2/H_2 chemistry in an HF-CVD reactor. This apparent dichotomy has been investigated further by the Moscow group using a realistic 3-D model of the Bristol HF-CVD reactor.[68,69] The full model comprises three blocks, describing gas phase processes (heat and mass transfer, chemical kinetics), gas–surface processes at the substrate (diamond growth mechanisms) and the activation processes (gas heating, H_2 dissociation on the filament), respectively. The gas phase kinetic and thermochemical information is provided by the GRI-Mech 3.0 detailed reaction mechanism for C/H/O mixtures,[24] modified by the exclusion of all reaction steps involving oxygen. Given that our particular objective is a better understanding of the gas phase chemistry, gas–surface chemistry at the substrate was omitted also. The reactor is represented in Cartesian co-ordinates, with the z axis parallel to the gas flow direction (*i.e.* inlet → outlet) and perpendicular to the long axis of the filament, y. The x axis is orthogonal to both the flow direction and the filament, and point (0,0,0) defines the centre of the filament. Experimental measurements as a function of d are thus directly comparable to model outputs along the axis $(0,0,+z)$, starting at $z = 1.5$ mm (the radius of the filament coil). Numerical integration of the conservation equations for mass, momentum, energy and species number densities, with the appropriate initial and boundary conditions, thermal and caloric equations of state, until steady state conditions are attained, yielded spatial distributions of T_{gas}, the flow field and the number densities of the various species. Variables in the calculation are the net H atom production rate, Q, at the filament surface, and the temperature drop, ΔT, between the filament surface and the gas in the immediate vicinity of the surface. The solid and dashed curves in Fig. 9(c) demonstrate how well the 3-D model (with gas pressures, flow rates and filament parameters appropriate to the Bristol HF-CVD reactor) is able to reproduce the experimentally determined variation of $[CH_3]$ with d for both the 1% CH_4 in H_2 and 0.5% C_2H_2 in H_2 gas mixtures if we assume reasonable values for $Q = +6 \times 10^{18}$ cm^{-2} s^{-1} and $\Delta T = 475$ K (*i.e.* the near-filament gas temperature, $T_{nf} = 2000$ K).

With these parameters established, we are now in a position to model, and rationalise, the detailed chemistry prevailing in HF activated dilute C_2H_2/H_2 gas mixtures. Careful inspection of the GRI-Mech 3.0 gas phase reaction mechanism[24]—key elements of which are listed in Table 3—reveals large variations in the chemistry prevailing in different regions of the reactor. Far from the filament, [H] is still significant (recall Fig. 6), but T_{gas} is low. As Table 3 shows, atomic hydrogen drives $C_2 \rightarrow C_1$ conversion *via* this multi-step sequence of reactions at low gas temperatures (*e.g.* 735 K) whereas, at much higher T_{gas} values, the reverse process dominates.[69]

Table 3 Major elementary steps (9)–(29) included in the $C_2 \rightarrow C_1$ conversion mechanism, together with their respective reaction rates at the specified gas temperatures calculated using the 3-D model for an input gas mixture of 0.5% C_2H_2 in H_2 and 20 Torr total pressure. M represents a third body. The calculated H atom number densities at these gas temperatures are, respectively, 1.6×10^{14} cm^{-3} (730 K), 4.1×10^{14} cm^{-3} (1200 K), 5.7×10^{14} cm^{-3} (1750 K) and 6.2×10^{14} cm^{-3} (2000 K). The net rates of various conversions under these respective conditions are shown in bold

Reaction number	Reaction	Reaction rate/cm^{-3} s^{-1}			
		730 K	1200 K	1750 K	2000 K
9	$H + C_2H_2 + M \rightarrow C_2H_3 + M$	1.85E + 16	4.00E + 15	4.07E + 14	1.64E + 14
10	$C_2H_3 + M \rightarrow H + C_2H_2 + M$	3.72E + 12	1.23E + 15	1.93E + 16	3.23E + 16
11	$H + C_2H_3 \rightarrow H_2 + C_2H_2$	1.05E + 16	3.34E + 15	5.24E + 15	6.07E + 15
12	$H_2 + C_2H_2 \rightarrow H + C_2H_3$	7.15E + 1	2.54E + 9	8.58E + 12	6.97E + 13
	Total: $C_2H_2 \rightarrow C_2H_3$	**8.00E + 15**	**−5.73E + 14**	**−2.41E + 16**	**−3.82E + 16**
13	$H + C_2H_4 \rightarrow H_2 + C_2H_3$	7.73E + 13	7.99E + 15	5.78E + 16	9.71E + 16
14	$C_2H_3 + H_2 \rightarrow H + C_2H_4$	7.64E + 15	7.86E + 15	3.35E + 16	5.47E + 16
15	$H + C_2H_3 + M \rightarrow C_2H_4 + M$	3.12E + 14	2.21E + 13	8.58E + 12	5.93E + 12
16	$C_2H_4 + M \rightarrow H + C_2H_3 + M$	0	5.25E + 6	1.15E + 12	2.38E + 13
	Total: $C_2H_3 \rightarrow C_2H_4$	**7.87E + 15**	**−1.10E + 14**	**−2.42E + 16**	**−4.25E + 16**
17	$C_2H_4 + M \rightarrow H_2 + C_2H_2 + M$	4.14E + 1	8.76E + 10	5.94E + 14	4.40E + 15
18	$H + C_2H_4 + M \rightarrow C_2H_5 + M$	5.02E + 15	6.14E + 14	3.55E + 13	1.20E + 13
19	$C_2H_5 + M \rightarrow H + C_2H_4 + M$	3.15E + 11	2.29E + 14	1.47E + 15	1.52E + 15
20	$H + C_2H_5 \rightarrow H_2 + C_2H_4$	4.32E + 13	4.01E + 13	3.13E + 13	2.37E + 13
21	$H_2 + C_2H_4 \rightarrow H + C_2H_5$	0	2.50E + 7	5.88E + 10	4.25E + 11
	Total: $C_2H_4 \rightarrow C_2H_5$	**4.97E + 15**	**3.45E + 14**	**−1.47E + 15**	**−1.53E + 15**
22	$CH_3 + CH_3 + M \rightarrow C_2H_6 + M$	4.22E + 14	2.77E + 14	3.30E + 13	1.13E + 13
23	$C_2H_6 + M \rightarrow CH_3 + CH_3 + M$	6.74E + 2	5.09E + 11	8.01E + 14	3.02E + 15
24	$CH_3 + CH_3 \rightarrow H + C_2H_5$	3.73E + 11	3.25E + 13	1.47E + 14	1.80E + 14
25	$H + C_2H_5 \rightarrow CH_3 + CH_3$	5.39E + 15	4.82E + 15	3.13E + 15	2.18E + 15
	Total: $C_2H_6/C_2H_5 \rightarrow CH_3$	**4.97E + 15**	**4.51E + 15**	**3.75E + 15**	**5.00E + 15**
26	$H + C_2H_6 \rightarrow H_2 + C_2H_5$	5.94E + 14	4.55E + 15	4.76E + 15	3.86E + 15
27	$C_2H_5 + H_2 \rightarrow H + C_2H_6$	7.34E + 12	8.57E + 13	3.24E + 14	3.97E + 14
28	$H + C_2H_5 + M \rightarrow C_2H_6 + M$	1.63E + 14	1.70E + 13	1.50E + 12	4.98E + 11
29	$C_2H_6 + M \rightarrow H + C_2H_5 + M$	0	2.10E + 8	1.71E + 12	1.10E + 13
	Total: $C_2H_6 \rightarrow C_2H_5$	**4.23E + 14**	**4.45E + 15**	**4.44E + 15**	**3.48E + 15**

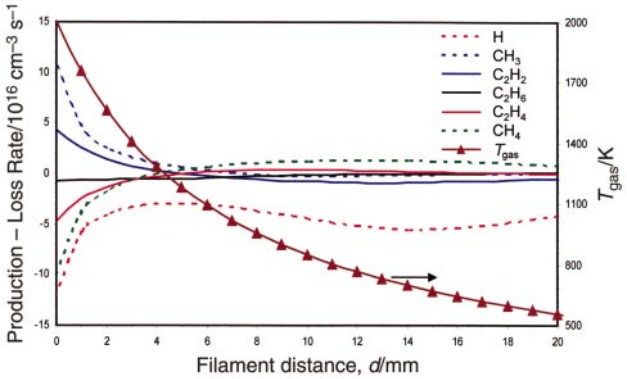

Fig. 10 Plot showing the d dependence of the source terms (*i.e.* production minus loss terms in the gas phase reaction mechanism) for the more abundant hydrocarbon species indicated in the legend, calculated *via* 3-D modelling (at 1 mm intervals) of the Bristol HF-CVD reactor operating with a 0.5% C_2H_2 in H_2 gas mixture, 20 Torr total pressure and with $T_{fil} = 2475$ K.

These findings are summarised in Fig. 10, which shows the calculated d dependence of T_{gas} and the various source terms (*i.e.* production minus loss terms in the gas phase reaction mechanism) for key hydrocarbon species in the Bristol

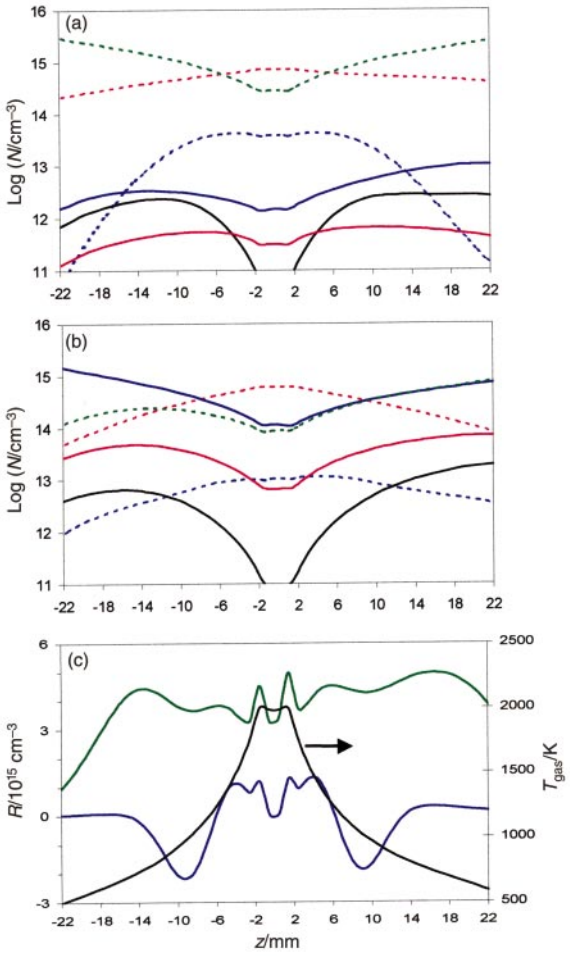

Fig. 11 Plots showing the z dependence of [H], [CH_3], [CH_4], [C_2H_2], [C_2H_4] and [C_2H_6] number densities, N (calculated at 1 mm grid spacings), for input gas mixtures comprising (a) 1% CH_4 in H_2 and (b) 0.5% C_2H_2 in H_2. Both assume a total pressure of 20 Torr, a flow rate of 100 sccm, a near filament gas temperature, $T_{nf} =$ 2000 K and a net H atom production rate at the filament, $Q = 6 \times 10^{18}$ cm^{-2} s^{-1} (*i.e.* as for the calculations shown in Fig. 9 and 10). Individual species are colour coded as per the legend in Fig. 10). (c) shows the calculated z dependence of the gas temperature profile and R, the net $C_2 \rightarrow C_1$ conversion rates under these conditions for CH_4/H_2 (blue) and C_2H_2/H_2 (green) gas feeds.

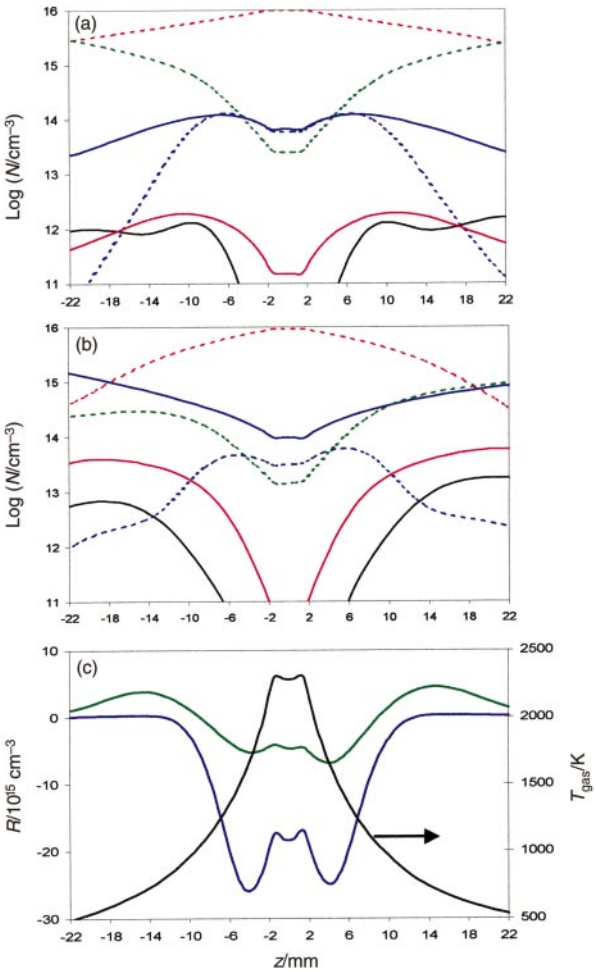

Fig. 12 Equivalent plots to those shown in Fig. 11, but with $T_{nf} =$ 2300 K and $Q = 1.2 \times 10^{20}$ cm^{-2} s^{-1}. Note the different order of magnitude for R under these more highly activated conditions.

HF-CVD reactor operating with a 0.5% C_2H_2 in H_2 gas mixture. This clearly shows $C_2 \rightarrow C_1$ conversion maximising at $d \sim 12$ mm, *i.e.* in regions far from the HF, where the gas temperatures are in the range 600–900 K. $C_2 \rightarrow C_1$ conversion proceeds as follows: gas phase C_2H_2 molecules in the presence of H atoms react to form other hydrocarbons ($C_2H_2 \rightarrow C_2H_3 \rightarrow C_2H_4 \rightarrow C_2H_5 \rightarrow CH_3 \rightarrow CH_x$, $x = 0, 1, 2, 4$ and $C_2H_6 \rightarrow C_2H_5$) in the cooler regions remote from the filament. Our analysis shows that approximately half of the C_2H_2 molecules that participate in the reactions convert to CH_3 radicals, while the remainder are reduced to C_2H_4.[69] The three-body recombination

$$H + CH_3 + M \rightarrow CH_4 + M \qquad (30)$$

is sufficiently fast at low T_{gas} to be an efficient source of CH_4 molecules, which can diffuse into the near filament region and re-convert to CH_3 radicals *via* the 'traditional' abstraction reaction (8). C_2H_4 molecules formed *via* reactions (9) and (14), which are very effective in cool regions of the reactor, undergo a similar series of transformations. Those that diffuse towards the hotter regions near the filament re-convert to C_2H_2, primarily *via* a multi-step mechanism dominated by reactions (13), (10) and (11). The resulting C_2H_2 molecules can in turn diffuse to cooler parts of the reactor where they may be further recycled to CH_3 (and thus CH_4) and C_2H_4. Unimolecular decay of C_2H_6 (reaction (23)) makes a significant contribution to $C_2 \rightarrow C_1$ conversion very close to the HF. Interconversion between the various hydrocarbon species also occurs rapidly in this region, since both [H] and T_{gas} are large. However, the 'near filament' volume is small and the overall

extent of species conversion in this region is more than counter-balanced by slower, reverse conversions in the cooler, but much more voluminous, regions distant from the HF. Diffusion provides the means of species transport. $C_2 \rightarrow C_1$ conversion times under typical HF-CVD reactor conditions are very sensitive to the local H atom number density, but are generally in the range 10^{-2}–10^{-1} s; as such, they are much longer than the times required for the fast hydrogen shift reactions that establish the partitioning between the various members of the C_1H_x and C_2H_x families.

Fig. 11 and 12 provide further visualisations of the calculated spatial variation in the number densities of H atoms and various of the key hydrocarbon species, the gas temperature, and $C_2 \rightarrow C_1$ interconversion rates within an HF-CVD reactor such as those used in Bristol, for both 1% CH_4 in H_2 and 0.5% C_2H_2 in H_2 gas mixtures. The two sets of calculations both assume a total pressure of 20 Torr and a flow rate of 100 sccm, but very different values of the near-filament gas temperature T_{nf} (and Q). The number densities shown in Fig. 11 are for $T_{nf} = 2000$ K and $Q = 6 \times 10^{18}$ cm^{-2} s^{-1} (*i.e.* as for the calculations shown in Fig. 9 and 10), while those in Fig. 12 are appropriate for $T_{nf} = 2300$ K and $Q = 1.2 \times 10^{20}$ cm^{-2} s^{-1} (a representative value when operating with a W filament at high temperature). Each figure consists of three panels. The first two show, respectively, the calculated z dependence of the various number densities, N, when using (a) 1% CH_4 in H_2 and (b) 0.5% C_2H_2 in H_2; note the obvious and inevitable asymmetry (about $z = 0$) in, for example, $[CH_4]$ in the case of a C_2H_2/H_2 input gas mixture. The third panel (c) displays the corresponding variation in the gas temperature and $C_2 \rightarrow C_1$ interconversion rates with z. These serve to emphasise not just the inhomogeneity of the gas phase composition within an HF-CVD reactor but also the similarity in relative species concentrations (particularly at the higher Q value), both in the immediate vicinity of the HF and in the region $z = 6$–10 mm where diamond deposition would typically occur, irrespective of the particular choice of hydrocarbon source gas.

III. Growth from C/H/O-containing gas mixtures

From the earliest days of diamond CVD, chemists have been exploring the use of alternatives to simple hydrocarbon/H_2 gas mixtures in the quest for improved growth rates, improved film quality, or lower deposition temperatures. The literature contains many reports of diamond CVD from C and H-containing gas mixtures that have been supplemented by small amounts of O_2 or other oxygen containing compounds—usually in a microwave reactor, since even trace amounts of oxygen tend to cause oxidation and rapid destruction of hot metal filaments.[70–72] Bachmann *et al.*[9,10] analysed the results of many such deposition experiments, using different process gas mixtures and reactor types, which they summarised within the framework of an atomic C/H/O phase diagram similar to that shown in Fig. 13. Their analysis led to the realisation that successful diamond growth is only possible within a well-defined small region of compositional space where the ratio of the carbon to oxygen mole fraction in the gas mixture, $X(C)/X(O)$, is ~ 1. This is depicted by the red tie line joining the point representing 100% hydrogen (*i.e.* the left-hand apex) to the point representing 100% pure CO (the mid-point of the opposite side of the triangle). All possible H/CO mixing ratios lie along this tie line. Use of gas mixtures in which $X(C)/X(O)$ is significantly greater than unity results in the formation of poor quality diamond or non-diamond carbon films while, for $X(C)/X(O) < 1$, no deposition is observed.

As with the preceding discussions of hydrocarbon/H_2 chemistry, we first consider such observations in the light of equilibrium thermodynamics. Consider the oxidation of methane and acetylene—the most plentiful hydrocarbons in most CVD

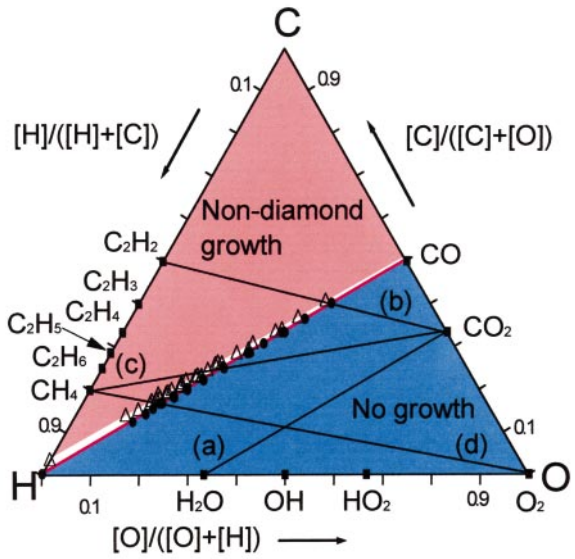

Fig. 13 C/H/O atomic phase diagram (after ref. 9 and 10). The white region lying above the H–CO tie line represents the diamond growth domain found experimentally, while no growth and non-diamond carbon growth regions are indicated in blue and pink, respectively. The H–CO tie line is shown in red, while tie lines spanning all possible mixing ratios of each of the four gas mixtures (CO_2/H_2O, CO_2/C_2H_2, CO_2/CH_4 and O_2/CH_4) explicitly discussed in the text are shown as (——). (●) indicates the input composition at which, for any given gas mixture, the methyl radical mole fraction, $X(CH_3)$ shows a step increase from $\sim 10^{-10}$ to $\sim 10^{-6}$, while (△) shows the compositions for which $[H]/[C_2H_2] = 0.2$ at $T_{gas} = 2000$ K.

environments:

$$2CH_4 + O_2 \rightleftharpoons 2CO + 4H_2 \quad (31)$$

and

$$C_2H_2 + O_2 \rightleftharpoons 2CO + H_2. \quad (32)$$

$\Delta_r G$ for both of these multi-step transformations is large and negative at all temperatures of interest in diamond CVD (see Table 2). The respective equilibria thus lie far to the right, ensuring that, in each case, the minority reactant will be fully consumed. Thus we arrive at a qualitative rationale for the observations of Bachmann *et al.*[9,10] When the $X(C)/X(O)$ ratio is just greater than unity, the activated process gas mixture will consist of a small amount of residual hydrocarbon in a background gas mixture of CO and H_2. Assuming that CO itself does not contribute to diamond growth, this mixture has much in common with the standard oxygen-free gas mixtures discussed above. Diamond deposition can occur and, as with the traditional hydrocarbon/H_2 mixtures, film quality will be compromised if the concentration of 'free' hydrocarbon gets too high. Conversely, when $X(C)/X(O) < 1$, the hydrocarbon source gas is entirely converted to CO and there are no 'active' C_1 species to promote film growth.[73]

More quantitative investigations of the gas phase chemistry prevailing in such reaction mixtures remain rare, however. A number of groups have used wavelength dispersed optical emission spectroscopy (OES) to follow variations in the relative intensities of emitting species in C/H/O containing plasmas (*e.g.* CH, C_2 radicals) with, for example, the input gas mixing ratio and/or with the quality of the deposited film.[74–76] Most recent attention in this particular area has been focused on the use of CO_2/CH_4 gas mixtures in microwave plasma enhanced CVD, following reports that this provided a route to depositing high quality diamond at lower substrate temperatures.[77,78] The process window using this gas mixture is found to be narrow, and centred at a composition of 50% CO_2/50%CH_4 by volume flow rate.[75,76] Such

observations accord with the criterion that $X(C)/X(O) \sim 1$ for optimum quality diamond growth, but provide little in the way of new insight into the detailed chemistry prevailing with such gas mixtures.

The Bristol group have used a combination of *in situ* molecular beam mass spectrometry and theoretical modelling using SENKIN (part of the CHEMKIN suite of computer programs[79]) to unravel aspects of the chemistry prevailing in a microwave plasma enhanced diamond CVD reactor operating with CO_2/CH_4 gas mixtures.[11] CO_2, CO, H_2O, H_2, CH_4 and C_2H_2 molecules, and CH_3 radicals, are all present in sufficient abundance to allow experimental monitoring of the way in which their relative number densities vary with CO_2/CH_4 mixing ratio. Illustrative results are shown in Fig. 14, along with the results of the SENKIN simulations. The latter calculations, which were performed for the complete range of CO_2/CH_4 mixing ratios, included all relevant reactions of H, C and O containing species and temperature dependent rate constants as tabulated in the GRI-Mech 3.0 gas phase reaction mechanism, but assumed a single gas temperature (2000 K), pressure (40 Torr) and interaction time (5 s), and did not allow for any transport in or out of the reaction volume.[11] The foregoing description of the 3-D modelling of hydrocarbon/H_2 gas mixtures serves to highlight the potential limitations of such zero-dimensional calculations, though previous TALIF measurements[53] of H atom Doppler lineshapes in a similar MW reactor (admittedly operating with hydrocarbon/H_2 gas mixtures) indicate much shallower temperature gradients than in the HF-CVD reactor. As Fig. 14 shows, the 0-D calculations actually do succeed in capturing many of the key trends observed experimentally. Specifically, CH_4 addition is seen to cause efficient scavenging of CO_2, to the extent that once the CH_4 input mole fraction exceeds $\sim$0.4, CO_2 is no longer detectable in the plasma region even though it still accounts for some 60% of the input gas mixture. Signals due to CO, H_2O and H_2 are all observed to rise as the CH_4/CO_2 input gas ratio increases. The H_2O signal peaks when CH_4 constitutes about 20% of the input gas mixture, while CO is seen to maximise at somewhat higher $X(CH_4)$ input mole fractions. Measured H_2 appears to scale with the input CH_4 volume fraction of CH_4, while CH_4, CH_3 and C_2H_2 signals are only detected in the plasma once the input gas ratio, $X(CH_4)/X(CO_2)$, has reached $\sim$1. The GRI-Mech 3.0 database used in the simulations includes 29 C, H and O containing atomic and molecular species, and over 200 elementary reactions.[11] A small number of 'composite reactions' suffice to explain most of the observed trends, however. At low $X(CH_4)$, CO_2 is reduced both by a multi-step transformation summarised reaction (33) and, as the concentration of H_2 product increases, by the multi-step conversion (34), *i.e.*

$$CO_2 + CH_4 \rightleftharpoons 2CO + 2H_2 \quad (33)$$

$$CO_2 + H_2 \rightleftharpoons CO + H_2O. \quad (34)$$

The $\Delta_r G$ values for both transformations are negative at high temperatures (Table 2) and the equilibria lie well to the right. Such composite reactions account for the observed fall in measured CO_2 and the rise in the CO, H_2 and H_2O signals with increasing $X(CH_4)$. Once the input $X(CH_4)/X(CO_2)$ ratio exceeds some critical value, however, all of the CO_2 will have

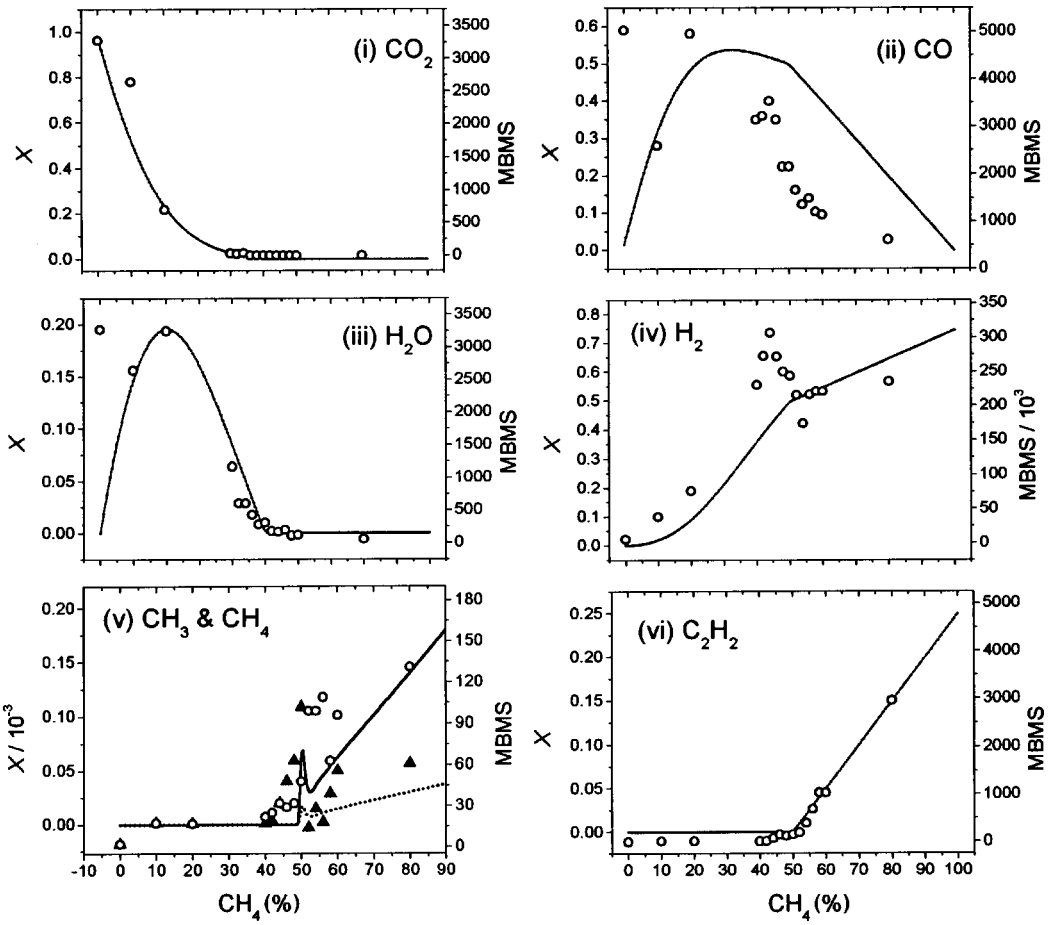

Fig. 14 Measured signal counts for (i) CO_2, (ii) CO, (iii) H_2O, (iv) H_2, (v) CH_3 and CH_4 and (vi) C_2H_2 when using MBMS to sample CO_2/CH_4 gas mixtures at 40 Torr total pressure activated with 1.2 kW of microwave radiation, plotted as a function of $\%CH_4$ in the input gas mixture. Individual data points are shown as (○) and, in the case of CH_3, by (▲), and link with the right-hand axis. The smooth black curves (dashed line for CH_3) show the corresponding calculated mole fractions, X, (left-hand scale) for each of these species obtained from the SENKIN simulations assuming a pressure of 40 Torr and $T_{gas} = 2000$ K.

been 'mopped up' and any remaining CH_4 is available to participate in alternative chemistry. Key composite reactions identified in the 'high $X(CH_4)$' regime include

$$2CH_4 \rightleftharpoons C_2H_2 + 3H_2 \quad (35)$$

and

$$C_2H_2 + H_2O \rightleftharpoons CH_4 + CO. \quad (36)$$

The former explains the fact that C_2H_2 is observed only when the input $X(CH_4) > 0.5$, while competition between the multi-step transformations (35) and (36) serves to account for the observed peak in the measured CH_4 and CH_3 signals at $X(CH_4)/X(CO_2)$ ratios slightly above unity. As Fig. 15 illustrates in expanded detail, increasing the CH_4/CO_2 ratio in the input gas mixture leads to a reduction in $X(CO_2)$ and thus, *via* transformation (34), a reduction in $X(H_2O)$. At the same time, however, composite reaction (35) results in an increase in $X(C_2H_2)$. Formation of active C_1 hydrocarbon species *via* conversion (36) depends on the concentration of both H_2O (which decreases with increasing input CH_4) and C_2H_2 (which increases with increasing input CH_4), and starts to contribute as soon as $X(CH_4)/X(CO_2)$ exceeds unity. This narrow region of compositional space, where the concentrations of CH_4 (and thus CH_3) start to increase but $X(C_2H_2)$ remains small, corresponds to the diamond growth window.[11,75,76] At higher input $X(CH_4)$, CH_3 is still present but, as a source of carbon for film growth, its effect is swamped by the excess of C_2H_2 with the consequence that, as in traditional hydrocarbon/H_2 chemistry, the deposited films become progressively more graphitic in character.[9]

Clearly, such comparatively crude zero-dimensional simulations are open to a number of criticisms. The assumption of a single gas temperature is unphysical, though the value chosen ($T_{gas} = 2000$ K) accords well with values derived from analysis of H atom TALIF lineshapes and CARS spectra of H_2 in a pure hydrogen plasma at comparable microwave power densities,[53] and from fitting the wavelength dependent continuum emission from a CH_4/CO_2 plasma in the Bristol microwave CVD reactor in terms of a blackbody distribution function.[76] Increasing or decreasing T_{gas} by 250 K gives demonstrably poorer agreement with the experimental measurements. No specific plasma induced chemistry is included in our modelling. Simply on energetic grounds, we expect bond fission (and radical formation) processes to be more abundant than ionization events, but the outputs of test simulations incorporating plasma induced radical forming reactions (with arbitrary weightings) show no significant differences to those reported above—a reflection of the rapidity of the thermochemical

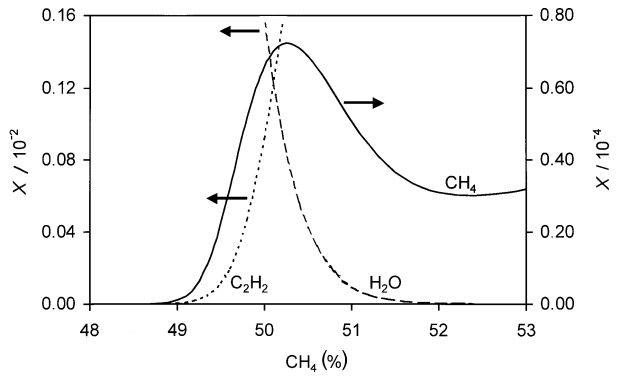

Fig. 15 Detail of the calculated compositional variation of the H_2O and C_2H_2 mole fractions (left-hand scale) and CH_4 mole fraction (right-hand axis) when using near equimolar CO_2/CH_4 gas mixtures at a total pressure of 40 Torr and $T_{gas} = 2000$ K. $X(CH_4)$ (and thus $X(CH_3)$ also) peaks at CO_2/CH_4 input mixing ratios very close to 1, where diamond growth is found to be optimal.

transformations occurring in a CH_4/CO_2 plasma at 2000 K. Finally, we recognise that the residence time used in the simulations ($\tau = 5$ s)[11] is some 50 times longer than would be expected for (say) a CH_3 radical diffusing through a CH_4/CO_2 plasma at 40 Torr total pressure. Simulations using ($\tau = 1$ s) are found to match the experimental measurements equally well, but calculations in which τ is reduced by another order of magnitude fail to reproduce many of the experimental trends shown in Fig. 14. These results hint at a need for further investigation of species transport in a plasma maintained close above a large (*i.e.* 10 cm diameter) platen surface.

The degree of insight provided by these simulations of the chemistry prevailing in CO_2/CH_4 gas mixtures encouraged a more wide-ranging modelling study of the chemistry of a wide variety of C/H/O containing gas mixtures, under conditions relevant to diamond CVD.[80] All combinations of the following hydrocarbon reactants: CH_4, C_2H_2, C_2H_3, C_2H_4, C_2H_5 and C_2H_6, with each of the species CO, CO_2, O_2, H_2O, OH and HO_2 were considered. Fig. 16 shows calculated mole fractions of H atoms, CH_3 radicals, and H_2, C_2H_2 and CO molecules for four illustrative gas mixtures: CO_2/H_2O, CO_2/C_2H_2, CO_2/CH_4 and O_2/CH_4, over the full compositional range, again assuming $T_{gas} = 2000$ K. As Fig. 16(a) shows, the CO_2/H_2O gas mixture is relatively unreactive. $X(CH_3)$ is predicted to be negligible ($<10^{-10}$) at all CO_2/H_2O mixing ratios, as is $X(C_2H_2)$—not surprisingly, given that this is the most stable product from CH_3 radical recombination. Such findings are consistent with expectations based on the C/H/O atomic phase diagram (Fig. 13), which shows the CO_2–H_2O tie line lying entirely within the no growth region, and are not changed by the inclusion of a realistic degree of plasma induced radical formation. In contrast, the CO_2–C_2H_2, CO_2–CH_4 and O_2–CH_4 tie lines each intercept the diamond growth region and, as Fig. 16 shows, hydrocarbon addition in each case results in a step change in $X(CH_3)$, from $\sim 10^{-10}$ to $>10^{-7}$, on passing through the composition where the $X(C)/X(O)$ ratio starts to exceed unity. In each case, $X(C_2H_2)$ mirrors the jump in $X(CH_3)$. This composition would thus be expected to represent the start of the diamond growth region—a view confirmed by experiment in the case of both CO_2/C_2H_2[74] and CO_2/CH_4[9–11,74–76] gas mixtures.

The upper boundary, separating the diamond growth domain from the large region of compositional space in which non-diamond deposition occurs, is less easy to define, not least because different groups may have different criteria for deciding what constitutes 'good quality' CVD diamond. Less debatable, however, is the assumption that growth of 'good quality' diamond will require a certain minimum concentration of gas phase H atoms to satisfy the various critical functions these perform, *i.e.* creating and re-terminating sites on the growing diamond surface, and etching non-diamond carbon in the deposited film. Such non-diamond growth is generally associated with higher than optimal concentrations of unsaturated hydrocarbons in the process gas mixture. C_2H_2 is by some way the most abundant hydrocarbon arising in these simulations, so we chose to focus on the ratio $X(H)/X(C_2H_2)$, and to require that it exceed some critical value in the simulations in order that 'good quality' diamond be deposited.[80] Inspection of the model output for all gas mixtures investigated, in the light of the available experimental data,[9–11,74] led to our adopting a value $X(H)/X(C_2H_2) = 0.2$, at the presumed gas temperature, $T_{gas} = 2000$ K. Note that this value is appropriate to the conditions assumed in the present (limited) simulations; the true mole fraction ratio at a growing diamond surface is likely to be very much smaller because of the rapid fall in T_{gas} in the boundary layer separating the bulk of the plasma from the substrate. We have already commented that CO_2/H_2O gas mixtures yield very little CH_3 (and thus C_2H_2); the $X(H)/X(C_2H_2)$ ratio for this

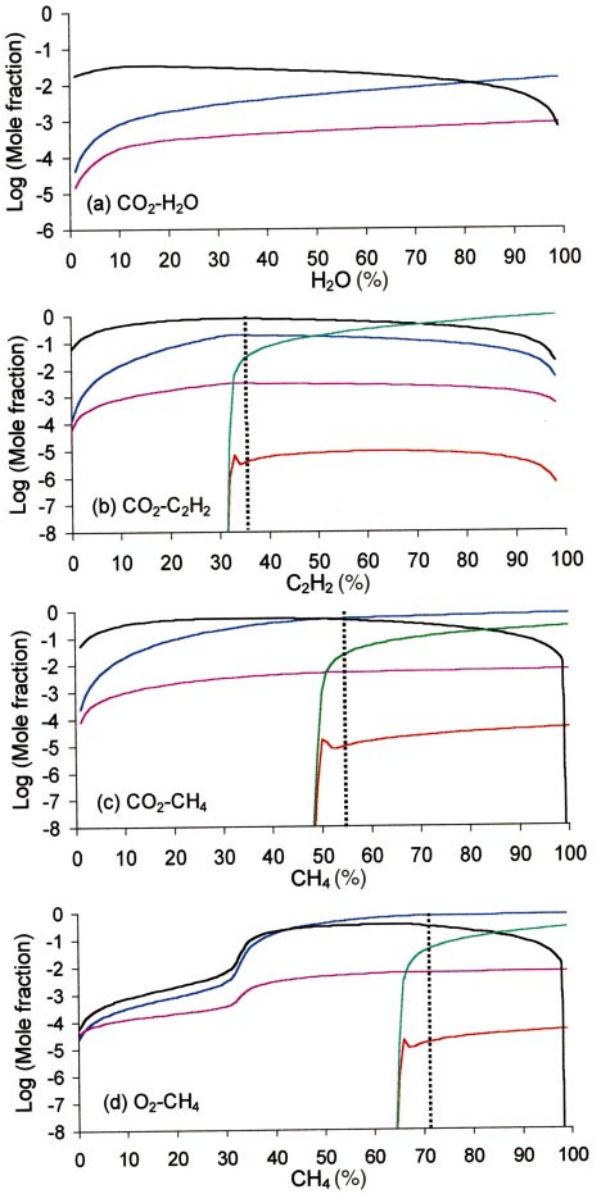

Fig. 16 Calculated species mole fractions, X, of C_2H_2 (green line), CO (black), CH_3 (red), H_2 (blue) and H atoms (pink) over the full compositional range for four different C/H/O containing input gas mixtures at $T_{gas} = 2000$ K: (a) CO_2/H_2O, (b) CO_2/C_2H_2, (c) CO_2/CH_4 and (d) O_2/CH_4. The input gas mixing ratio for which the calculated ratio $X(H)/X(C_2H_2) = 0.2$ is indicated by the dashed vertical line in (b)–(d); $X(H)/X(C_2H_2) \gg 0.2$ for all CO_2/H_2O mixing ratios.

mixture is much larger than 0.2 for all input gas compositions. For the other three gas mixtures the $X(H)/X(C_2H_2)$ ratio is also large for small additions of hydrocarbon, but declines rapidly as soon as the $X(C)/X(O)$ ratio in the feed-stock gas approaches unity and the concentrations of CH_3, and thus C_2H_2, start to build up. Clearly, the criterion adopted for the diamond/non-diamond growth boundary is somewhat arbitrary, but the form of the ratio (if not its absolute value which, in any case, is temperature dependent[80]) is physically defensible, and it provides a rationale for the observed upper limit to the diamond growth domain in the C/H/O atomic phase diagram.

IV. Conclusions

This Article provides a selective overview of the range of spectroscopic methods applied to studies of the gas phase chemistry involved in diamond CVD using traditional laboratory scale reactors. Experiment and theory are advancing in tandem, and much of the essential gas phase chemistry is now determined and understood. Questions remain, however, particularly in the case of MW-CVD reactors. Experiments which provide detailed spatially resolved measures of the temperature distribution or of the number densities of individual species within, and at the periphery of, the plasma ball in a MW-CVD reactor[53] remain rare. Microwave and other plasma CVD environments contain significant concentrations of ions (and electrons) which are likely to preclude use of REMPI probing methods, but absorption techniques like CRDS and, in the case of H atoms, measurement of THG signals[14] may yet provide such information. Detailed studies of the gas phase chemistry prevailing in both HF and MW-CVD reactors when operating with other than C, H (and O)-containing gases—such as are used when attempting B-, N- or S-doped CVD diamond deposition—are similarly missing. Some such investigations are now starting in Bristol, however. Moving beyond pure gas phase chemistry, a full understanding of diamond CVD also requires better parametrisation of the gas–surface reactions, most notably the loss of, for example, H atoms and hydrocarbon radicals at the growing diamond surface, and the way these processes depend on factors like the substrate temperature, surface morphology, *etc.*[81–85] Our recent studies of diamond growth from MW plasma activated CO_2/CH_4 gas mixtures[11] served to confirm previous suggestions[77,78] that this provides a route to forming good quality CVD diamond at reduced substrate temperatures, T_{sub}. Consistent with this, our measurements of the variation in film growth rate with T_{sub} suggest an activation energy, E_{act}, for the film deposition process of $\sim$28 kJ mol^{-1} (analogous measurements on films grown from CH_4/H_2 gas mixtures give significantly higher E_{act} values[86,87]). Do CO molecules participate in the gas–surface chemistry in such reaction mixtures? The available literature appears contradictory on this point.[88,89] Such fundamental uncertainties provide clear indication of the need for further detailed research in this field.

Acknowledgements

We are grateful to EPSRC for equipment grants and for the award of a Senior Research Fellowship (MNRA) and a studentship (JAS), to De Beers Industrial Diamond Ltd. for their support of many aspects of this work and for an Industrial CASE studentship (JRP), to the Royal Society for travel grants to enable the Bristol–Moscow collaboration, to Drs. C. A. Rego, R. S. Tsang, S. M. Leeds and S. A. Redman and M. A. Elliott for their contributions to earlier stages of the research of the Bristol group, and to Drs J. E. Butler (Naval Research Laboratory, Washington, D.C.), A. J. Orr-Ewing and C. M. Western for their help and interest in this work.

References

1 *The Properties of Natural and Synthetic Diamond*, ed. J. E. Field, Academic Press, London, 1992.
2 B. V. Spitsyn, L. L. Builov and B. V. Derjaguin, *J. Cryst. Growth*, 1981, **52**, 219.
3 S. Matsumoto, Y. Sato, M. Kamo and N. Setaka, *Jpn. J. Appl. Phys.*, 1983, **21**, L183.
4 M. Kamo, Y. Sato, S. Matsumoto and N. Setaka, *J. Cryst. Growth*, 1983, **62**, 642.
5 D. G. Goodwin and J. E. Butler, in *Handbook of Industrial Diamonds and Diamond Films*, ed. M. A. Prelas, G. Popovici and L. K. Bigelow, Marcel Dekker, New York, 1998, pp. 527–581, and references therein.
6 R. J. H. Klein-Douwel and J. J. ter Meulen, *J. Appl. Phys.*, 1998, **83**, 4734.
7 A. G. Löwe, A. T. Hartlieb, J. Brand, B. Atakan and K. Kohse-Hoinghaus, *Combust. Flame*, 1999, **118**, 37.

8 K. Kohse-Hoinghaus, A. Löwe and B. Atakan, *Thin Solid Films*, 2000, **368**, 185.
9 P. K. Bachmann, D. Leers, H. Lydtin and D. U. Wiechert, *Diamond Relat. Mater.*, 1991, **1**, 1.
10 P. K. Bachmann, H. G. Hagemann, H. Lade, D. Leers, F. Picht and D. U. Wiechert, *Mater. Res. Soc. Symp. Proc.*, 1994, **339**, 267.
11 J. R. Petherbridge, P. W. May, S. R. J. Pearce, K. N. Rosser and M. N. R. Ashfold, *J. Appl. Phys.*, 2001, **89**, 1484, and references therein.
12 S. O. Hay, W. C. Roman and M. B. Colket, *J. Mater. Res.*, 1990, **5**, 2387.
13 K.-H. Chen, M.-C. Chuang, C. M. Penney and W. F. Banholzer, *J. Appl. Phys.*, 1992, **71**, 1485.
14 L. L. Connell, J. W. Fleming, H.-N. Chu, D. J. Vesteck, Jr., E. Jensen and J. E. Butler, *J. Appl. Phys.*, 1995, **78**, 3622.
15 V. Zumbach, J. Schafer, J. Tobai, M. Ridder, T. Dreier, B. Ruf, F. Behrendt, O. Deutschmann and J. Warnatz, *J. Chem. Phys.*, 1997, **107**, 5918.
16 K. L. Menningen, M. A. Childs, L. W. Anderson and J. E. Lawler, *Rev. Sci. Instrum.*, 1996, **67**, 1546.
17 F. G. Celii and J. E. Butler, *Annu. Rev. Phys. Chem.*, 1991, **42**, 643.
18 W. L. Hsu, *J. Vac. Sci. Technol. A*, 1988, **6**, 1803; W. L. Hsu, *J. Appl. Phys.*, 1992, **72**, 3102.
19 W. L. Hsu, M. C. McMaster, M. E. Coltrin and D. S. Dandy, *Jpn. J. Appl. Phys.*, 1994, **33**, 2231.
20 C. A. Rego, R. S. Tsang, P. W. May, M. N. R. Ashfold and K. N. Rosser, *J. Appl. Phys.*, 1996, **79**, 7264, and references therein.
21 C. A. Rego, P. W. May, C. R. Henderson, M. N. R. Ashfold, K. N. Rosser and N. M. Everitt, *Diamond Relat. Mater.*, 1995, **4**, 770.
22 C.-H. Wu, M. A. Tamor, T. J. Potter and E. W. Kaiser, *J. Appl. Phys.*, 1990, **68**, 4825.
23 T. Mitomo, T. Ohta, E. Kondoh and K. Ohtsuka, *J. Appl. Phys.*, 1991, **70**, 4532.
24 G. P. Smith, D. M. Golden, M. Frenklach, N. W. Moriarty, B. Eiteneer, M. Goldenberg, C. T. Bowman, R. K. Hanson, S. Song, W. C. Gardiner, Jr., V. V. Lissianski and Z. Qin, http://www.me.berkeley.edu/gri_mech/
25 N. Setaka, *J. Mater. Res.*, 1989, **4**, 664.
26 R. R. Rye, *Surf. Sci.*, 1977, **69**, 653.
27 A. B. King and H. Wise, *J. Phys. Chem.*, 1963, **67**, 1163.
28 R. K. Gould, *J. Chem. Phys.*, 1975, **63**, 1825.
29 J. Biener, U. A. Schubert, A. Schenk, B. Winter, C. Lutterloh and J. Kuppers, *J. Chem. Phys.*, 1993, **99**, 3125.
30 K. Tankala and T. DebRoy, *J. Appl. Phys.*, 1992, **72**, 712.
31 C. Wolden, S. Mitra and K. K. Gleason, *J. Appl. Phys.*, 1992, **72**, 3750.
32 H. Toyoda, M. A. Childs, K. L. Menningen, L. W. Anderson and J. E. Lawler, *J. Appl. Phys.*, 1994, **75**, 3142.
33 U. Meier, K. Kohse-Hoinghaus, L. Schafer and C.-P. Klages, *Appl. Opt.*, 1990, **29**, 4993.
34 L. Schafer, C.-P. Klages, U. Meier and K. Kohse-Hoinghaus, *Appl. Phys. Lett.*, 1991, **58**, 571.
35 A. D. Tserepi, J. R. Dunlop, B. L. Preppernau and T. A. Miller, *J. Appl. Phys.*, 1992, **72**, 2638.
36 M. Chenevier, J. C. Cubertafon, A. Campargue and J. P. Booth, *Diamond Relat. Mater.*, 1994, **3**, 587.
37 F. G. Celii and J. E. Butler, *Appl. Phys. Lett.*, 1989, **54**, 1031.
38 F. G. Celii, H. R. Thorsheim, J. E. Butler, L. S. Plano and J. M. Pinneo, *J. Appl. Phys.*, 1990, **68**, 3814.
39 M. N. R. Ashfold and J. D. Prince, *Mol. Phys.*, 1991, **73**, 297, and references therein.
40 M. A. Childs, K. L. Menningen, L. W. Anderson and J. E. Lawler, *J. Chem. Phys.*, 1996, **104**, 9111.
41 A. Gicquel, M. Chenevier, Y. Breton, M. Petiau, J. P. Booth and K. Hassouni, *J. Phys. III, France*, 1996, **6**, 1167.
42 S. A. Redman, C. Chung, K. N. Rosser and M. N. R. Ashfold, *Phys. Chem. Chem. Phys.*, 1999, **1**, 1415.
43 D. G. Goodwin and G. G. Gavillet, *J. Appl. Phys.*, 1990, **68**, 6393.
44 D. S. Dandy and M. E. Coltrin, *J. Appl. Phys.*, 1994, **76**, 3102.
45 K. Tankala and T. DebRoy, *J. Appl. Phys.*, 1992, **72**, 712.
46 R. Otsuka, M. Ihara and H. Komiyama, *J. Appl. Phys.*, 1995, **77**, 893.
47 Y. A. Mankelevich, A. T. Rakhimov and N. V. Suetin, *Diamond Relat. Mater.*, 1996, **5**, 888.
48 S. J. Harris and A. M. Weiner, *J. Appl. Phys.*, 1993, **74**, 1022.
49 I. Langmuir, *J. Am. Chem. Soc.*, 1915, **37**, 417.
50 M. W. Chase, Jr., C. A. Davies, J. R. Downey, Jr., D. J. Frurip, R. A. McDonald and A. N. Syverud, *J. Phys. Chem. Ref. Data*, 1985, **14**, Suppl. 1.
51 M. Sommer and F. W. Smith, *J. Mater. Res.*, 1990, **5**, 2433.
52 D. M. Li, R. Hernberg and T. Mäntylä, *Diamond Relat. Mater.*, 1998, **7**, 1709.
53 A. Gicquel, K. Hassouni, Y. Breton, M. Chenevier and J. C. Cubertafon, *Diamond Relat. Mater.*, 1996, **5**, 366.
54 M. A. Childs, K. L. Menningen, P. Chevako, N. W. Spellmeyer, L. W. Anderson and J. E. Lawler, *Phys. Lett. A*, 1992, **171**, 87.
55 U. Lommatzsch, E. H. Wahl, T. G. Owano, C. H. Kruger and R. N. Zare, *Chem. Phys. Lett.*, 2000, **320**, 339.
56 F. G. Celii, P. E. Pehrsson, H.-t. Wang and J. E. Butler, *Appl. Phys. Lett.*, 1988, **52**, 2043.
57 M. A. Childs, K. L. Menningen, H. Toyoda, Y. Ueda, L. W. Anderson and J. E. Lawler, *Phys. Lett. A*, 1994, **194**, 119.
58 F. G. Celii and J. E. Butler, *J. Appl. Phys.*, 1992, **71**, 2876.
59 E. J. Corat and D. G. Goodwin, *J. Appl. Phys.*, 1993, **74**, 2021.
60 J. Heinze, N. Heberle and K. Kohse-Hoinghaus, *Chem. Phys. Lett.*, 1994, **223**, 305.
61 J. A. Smith, M. A. Cook, S. R. Langford, S. A. Redman and M. N. R. Ashfold, *Thin Solid Films*, 2000, **368**, 169.
62 J. A. Smith, E. Cameron, M. N. R. Ashfold, Y. A. Mankelevich and N. V. Suetin, *Diamond Relat. Mater.*, 2001, **10**, 358, and references therein.
63 P. Zalicki, Y. Ma, R. N. Zare, E. H. Wahl, J. R. Dadamio, T. G. Owano and C. H. Kruger, *Chem. Phys. Lett.*, 1995, **234**, 269.
64 P. Zalicki, Y. Ma and R. N. Zare, *Appl. Phys. Lett.*, 1995, **67**, 144.
65 E. H. Wahl, T. G. Owano, C. H. Kruger, P. Zalicki, Y. Ma and R. N. Zare, *Diamond Relat. Mater.*, 1996, **5**, 373.
66 A. O'Keefe and D. A. G. Deacon, *Rev. Sci. Instrum.*, 1988, **59**, 2544.
67 M. D. Wheeler, S. M. Newman, A. J. Orr-Ewing and M. N. R. Ashfold, *J. Chem. Soc., Faraday Trans.*, 1998, **94**, 337, and references therein.
68 Y. A. Mankelevich, N. V. Suetin and A. T. Rakhimov, *Diamond Relat. Mater.*, 1998, **7**, 1133.
69 Y. A. Mankelevich, N. V. Suetin, M. N. R. Ashfold, J. A. Smith and E. Cameron, *Diamond Relat. Mater.*, 2001, **10**, 364.
70 T. Kawato and K. Kondo, *Jpn. J. Appl. Phys.*, 1987, **26**, 1429.
71 Y. Liou, A. Inspektor, R. Weimer, D. Knight and R. Messier, *J. Mater. Res.*, 1990, **5**, 2305.
72 S. Kapoor, M. A. Kelly and S. B. Hagstrom, *J. Appl. Phys.*, 1995, **77**, 6627.
73 R. Beckmann, B. Sobisch and W. Kulisch, *Diamond Relat. Mater.*, 1995, **4**, 256.
74 M. Marinelli, E. Milani, M. Montuori, A. Tebano and G. Balestrino, *J. Appl. Phys.*, 1994, **76**, 5702.
75 T. P. Mollart and K. L. Lewis, *Diamond Relat. Mater.*, 1999, **8**, 236.
76 M. A. Elliott, P. W. May, J. Petherbridge, S. M. Leeds, M. N. R. Ashfold and W. N. Wang, *Diamond Relat. Mater.*, 2000, **9**, 311.
77 C. F. Chen, S. H. Chen, H. W. Ko and S. E. Hsu, *Diamond Relat. Mater.*, 1994, **3**, 443.
78 J. Stiegler, T. Lang, M. Nygard-Ferguson, Y. von Kaenel and E. Blank, *Diamond Relat. Mater.*, 1996, **5**, 226.
79 R. J. Kee, F. M. Rupley and J. A. Miller, Sandia National Laboratories, Report SAND89-8009B, 1989.
80 J. R. Petherbridge, P. W. May and M. N. R. Ashfold, *J. Appl. Phys.*, 2001, **89**, 5219.
81 S. J. Harris, *Appl. Phys. Lett.*, 1990, **56**, 2298.
82 S. Skokov, B. Weiner and M. Frenklach, *J. Phys. Chem.*, 1994, **98**, 7073.
83 M. Frenklach and S. Skokov, *J. Phys. Chem. B*, 1997, **101**, 3025.
84 C. C. Battaile, D. J. Srolovitz and J. E. Butler, *J. Appl. Phys.*, 1997, **82**, 6293.
85 C. C. Battaile, D. J. Srolovitz, I. I. Oleinik, D. G. Pettifor, A. P. Sutton, S. J. Harris and J. E. Butler, *J. Chem. Phys.*, 1999, **111**, 4291, and references therein.
86 E. Kondoh, T. Ohta, T. Mitomo and K. Ohtsuka, *J. Appl. Phys.*, 1993, **73**, 3041.
87 H. Maeda, K. Ohtsubo, M. Irie, N. Ohya, K. Kusakabe and S. Morooka, *J. Mater. Res.*, 1995, **10**, 3115.
88 K. Itoh and O. Matsumoto, *Thin Solid Films*, 1998, **316**, 18.
89 S. C. Eaton and M. K. Sunkara, *Diamond Relat. Mater.*, 2000, **9**, 1320.
90 M. W. Chase, Jr., NIST-JANAF Thermochemical Tables, 4th edn., *J. Phys. Chem. Ref. Data*, 1998, Monograph No. 9, 1–1951.